Use of 2D-Video Disdrometer to Derive Mean Density-Size and Z_e-SR Relations: Four Snow Cases from the Light Precipitation Validation Experiment

Gwo-Jong Huang and V. N. Bringi

Colorado State University, Fort Collins, Colorado

Dmitri Moisseev

University of Helsinki and Finnish Meteorological Institute, Helsinki, Finland

W. A. Petersen and L. Bliven

NASA GSFC/Wallops Flight Facility, Wallops Island, VA

David Hudak
Environment Canada, Downsview, Ontario, CA

Submitted to Atmospheric Research

Submitted: February 2014

Corresponding author address: Gwo-Jong Huang, Colorado State University, Fort Collins, Colorado, CO 80525.
E-mail: gh222106@engr.colostate.edu

ABSTRACT

The application of the 2D-video disdrometer to measure fall speed and snow size distribution and to derive liquid equivalent snow rate, mean density-size and reflectivity-snow rate power law is described. Inversion of the methodology proposed by Böhm provides the pathway to use measured fall speed, area ratio and '3D' size measurement to estimate the mass of each particle. Four snow cases from the Light Precipitation Validation Experiment are analyzed with supporting data from other instruments such as Precipitation Occurrence Sensor System (POSS), Snow Video Imager (SVI), a network of seven snow gauges and three scanning C-band radars. The radar-based snow accumulations using the 2DVD-derived Z_e-SR relation are in good agreement with a network of seven snow gauges and outperform the accumulations derived from a climatological Z_e-SR relation used by the Finnish Meteorological Institute (FMI). The normalized bias between radar-derived and gauge accumulation is reduced from 96% when using the fixed FMI relation to 28% when using the Z_e-SR relations based on 2DVD data. The normalized standard error is also reduced significantly from 66% to 31%. For two of the days with widely different coefficients of the Z_e-SR power law, the reflectivity structure showed significant differences in spatial variability. Liquid water path estimates from radiometric data also showed significant differences between the two cases. Examination of SVI particle images at the measurement site corroborated these differences in terms of unrimed versus rimed snow particles. The findings reported herein support the application of Böhm's methodology for deriving the mean density-size and Z_e-SR power laws using data from 2D-video disdrometer.

1. Introduction

The measurement of liquid equivalent snow rate (*SR*) from radar has long been recognized as a difficult problem in quantitative precipitation estimation (QPE) but one of great importance for weather forecasting, hydrology, detection of aviation hazards and other remote sensing applications (e.g., ground validation for microwave radiometry from space). The validation of QPE by radar is difficult at best given the fact that accurate measurement of winter precipitation by gauges remains challenging due to the sheer variety and variability of physical properties which can change dramatically with, for example, relatively small changes in environmental conditions. Some of the important physical properties that one could list, for example, are (i) '3D'-size, (ii) terminal fall speed, (iii) particle size distribution, (iv) density (or, mass), (v) shape, (v) composition and (vi) porosity. Some of these attributes are not independent as evidenced by the large literature that exists in describing density (or, mass)-size and fall speed-size relations for different kinds of winter precipitation (e.g., Pruppacher and Klett 2010; Mason 2010). The fall speed is also dependent on shape, composition and porosity. Thus, it follows that fall speed is fundamental to characterization of frozen precipitation followed by a good measure of '3D'-size, particle size distribution and porosity. From the radar reflectivity perspective, the '3D'-size and associated size distribution and the density (or, mass)-size relation is of fundamental importance. For Rayleigh scattering the reflectivity is directly related to E[$m(D)^2$] where m is the particle mass and E stand for expectation or integration over the size distribution (Ryzhkov et al. 1998); however, the mass is not easily measured on a particle-by-particle basis. On the other hand, the liquid equivalent snow rate (*SR*) is directly related to E[$m(D)\ V_f(D)$]

where V_f is the fall speed. It follows that empirical Z_e-SR power laws can be derived if mass-D and V_f-D power laws are assumed (e.g., Matrosov et al. 2009) and the size distribution is measured (e.g., Sekhon and Srivastava 1970). The simulations of Matrosov et al. (2009) suggest that the overall uncertainty of estimating SR from reflectivity measurements can be as high as a factor of 3 or so. A more direct method is to correlate Z_e from radar with SR measured by snow gauges (e.g., Fujiyoshi et al. 1990 and references therein) which can lead to climatological Z_e-SR power law. The advent of optical-based surface disdrometers, however, has led to more accurate methods to characterize the physical properties of snow, leading to m-D, V_f-D and area ratio-D relations that are consistent via hydrodynamic theory (Böhm 1989; Mitchell 1996; Heymsfield and Westbrook 2010). Combined with scattering models (size, shape, dielectric constant), it leads to more consistent Z_e-SR power laws (Huang et al. 2011).

There are a number of disdrometers (mainly optical) that are available (some commercial and others in the research category) that measure a sub-set of the physical parameters listed above (only instruments that can image the particles are considered here). Hanesch (1999) and Schönhuber et al. (2000) used the 1st generation 2D-video disdrometer (2DVD) which measures fall speed and two orthogonal images from which an apparent volume (also, size distribution based on '3D'-size) as well as an estimate of porosity (via the area ratio to be described later) can be computed. Later, Brandes et al. (2007) used the 2DVD to estimate the coefficient and exponent of a mean density-D_0 power law (mainly for fluffy snow aggregates) by comparing 15-min liquid water accumulations with a collocated Geonor gauge (D_0 is the median volume diameter of the particle size distribution). They also examined the particle size distribution in detail by fitting with a gamma model and deriving correlations between the model parameters (e.g., shape parameter μ and slope parameter Λ). They conclude (in their Section 6, page 648) that, "…The video disdrometer is a powerful observational tool for studying the microphysical properties of winter storms". Further, Brandes et al. (2008) investigated power law relation between terminal fall speed and size and its dependence on temperature. The use of radar and 2DVD for estimating density-size and Z_e-SR power laws is described by Huang et al. (2010; 2011) whereas Zhang et al. (2011) demonstrated the importance of density-size power laws (empirically adjusted by fall speed) in comparing 2DVD-based reflectivity with ground radar. While the 2DVD is commercially available, a similar research instrument HVSD (Hydrometeor Velocity Size Detector; Barthazy et al. 2004) measures the fall speed and projected image in one plane. It has been used by Zawadzki et al. (2010) to investigate the natural variability of snow terminal velocity with size. They concluded that the exponent of the terminal velocity-D power law could be fixed at 0.18, while the coefficient is variable from event-to-event. Szyrmer and Zawadzki (2010) describe a methodology to derive the average relationship between terminal fall velocity and the mass of snowflakes via elaboration of the methodology of Böhm (1989) proposed by earlier Hanesch (1999); the latter used the 1st generation tall 2DVD design. In fact, the development of the HVSD by Barthazy et al. (2004) followed Hanesch and lead to a simpler instrument with two parallel light planes but with much slower line scan frequency camera. The work described herein follows Szyrmer and Zawadzki (2010) but uses the 2nd generation low profile 2DVD

(Schöenhuber et al. 2008) to derive the Z_e-SR power law with validation provided by a network of seven snow gauges.

Another research instrument is the Snow Video Imager (SVI; Newman et al. 2009) which, unlike the line scan camera, uses a CCD (charge-coupled device) full frame camera (60 frames per second) and images are obtained almost simultaneously; however, it does not measure the fall speed. SVI software yields a size estimate of each particle as an equivalent diameter that corresponds to a circular equivalent-area diameter of the irregular shape (with holes filled). Some advantages of the SVI over the 2DVD is that it has a large sample volume (twice that of the 2DVD), better pixel resolution (nominally 0.05 mm by 0.1 mm) and its measurements are less sensitive to wind. In this work, the SVI is mainly used to determine the particle size distribution for comparison with the 2DVD, and to examine samples of images to distinguish between unrimed and rimed snow particles. A new commercially available instrument is the Multi-Angle Snowflake Camera (MASC; Garrett et al. 2012) which gives high resolution (10-50 μm) photographs of snow particles from three viewing angles, along with their fall speed. One disadvantage is that the sample volume is small (about 1/10 of the 2DVD).

This article is organized as follows. In Section 2 the specific details of estimating the apparent volume and '3D'-apparent diameter, the adjusted particle size distribution and the application of Böhm's (1989) method are described. Section 3 constitutes the main bulk of the article and describes the 2DVD processing and derived products culminating in Z_e-*SR* power laws for the four snow days, comparison of liquid equivalent snow accumulations derived from radar with a network of 7 snow gauges, and radar-based accumulation maps. A short summary and conclusions are given in Section 4.

2. The basis for snow measurements using the 2D-video disdrometer

2.1 The apparent volume and diameter

The 2DVD gives two views (front and side views; actually silhouettes) of the particle in two orthogonal planes as shown in the example in Fig. 1. It is obvious that the 'true' volume of such an irregular particle cannot be calculated and thus we define here the apparent volume (VL_{app}) assuming that the particle is an ellipsoid. The apparent volume is defined as an average of two ellipsoidal volumes:

$$VL_{app} = \frac{\pi}{6} D_{app}{}^{3} = \frac{VL_{app1}+VL_{app2}}{2} \text{ ....(1)}$$

where the apparent diameter is D_{app} and,

$$VL_{app1} = \frac{\pi}{6}(H * W_1 * W_2) \text{ ....(2)}$$

where,

$$H = \sqrt{H_1 * H_2} \text{ ....(3a)}$$

$$W_{1,2} = \frac{4 * A_{e1,2}}{\pi * H} \text{ ....(3b)}$$

The $A_{e1,2}$ are the shadow areas (see Fig. 1) from the two views. The second ellipsoid estimate, VL_{app2}, is defined as:

$$VL_{app2} = \frac{\pi}{6}(HH * W_{max1} * W_{max2}) \text{ ....(4)}$$

where,

$$HH = \sqrt{HH_1 * HH_2} \text{ ....(5a)}$$

$$HH_{1,2} = \frac{4 * A_{e1,2}}{\pi * W_{max1,2}} \text{ ....(5b)}$$

In (5b) the W_{max} equals the maximum width of the scan line or 'slice' (measured from left to right in Fig. 1); the subscripts 1,2 refer to maximum width as determined from each view. The method of calculating VL_{app} and D_{app} here generally follows Hanesch (1999) which is somewhat different from Schönhuber et al. (2000) which was used later by Brandes et al. (2007). Also, the apparent diameter (D_{app}) is different from the 'size' measured by instruments that give the particle image in only one plane such as aircraft-mounted imaging probes (which give the top view). The 'size' is often defined as the maximum distance between two pixels or the diameter of the smallest circle that completely circumscribes the image or the equivalent-area diameter (Hogan et al. 2012). The latter also define the mean diameter as the mean of the particle dimensions in two orthogonal directions which they found to be better related to radar reflectivity. Since the true volume of snowflake is not known, the accuracy of our method of calculating VL_{app} cannot be determined. However, from the simulations of Wood et al. (2012) who used ellipsoidal shape models with canting it is can be inferred that the apparent diameter defined here gives a more 'realistic' measure of '3D' size made possible by the availability of two orthogonal images from the 2DVD.

2.2 Snow size distribution (SSD)

In a certain time window (typically 60 seconds for 1-minute averaged size distributions), all 'matched' snow particles are sorted into M size bins according to the apparent diameter (D_{app}) and the 'un-adjusted' size distribution $N_m(D_i)$ is computed as:

$$N_m(D_i) = \frac{1}{\Delta t * \Delta D} \sum_{j=1}^{N_i} \frac{1}{A_j * v_j} \qquad [mm^{-1}\, m^{-3}] \text{ ....(6)}$$

where D_i is the center diameter of the ith size bin (from 1 to M) in mm; ΔD is the bin width in mm; A_j is the measurement area in mm^2; v_j is the fall speed in m s^{-1} and Δt is the time window in seconds. The fall speed measurement is fundamental to the 2DVD and relies on the ability to match the particle that falls in the upper light plane (and is imaged by Camera A) to the same particle that falls through the lower light plane and is imaged by Camera B (see Fig. 2). The match criteria used here are adapted from Hanesch (1999) as elaborated by Huang et al. (2010). If the match criteria are not satisfied then that particle is rejected; it follows that the concentration will tend to be under-estimated. To re-adjust the measured $N_m(D_i)$ for this underestimate (assumed to be a constant factor γ) the following procedure is used.

Assume that snow falls uniformly over the instrument. Then, the theoretical number of snowflakes falling through the virtual measuring area divided by the theoretical number of snowflakes falling in the scan area of each camera (shown in Fig. 2) should be equal to the ratio of these two areas as:

$$\frac{theoretical\ \#\ of\ snowflakes\ in\ virtual\ measuring\ area}{theoretical\ \#\ of\ snowflakes\ in\ scan\ area\ of\ single\ camera} = \frac{100}{250} = 0.4 \text{ ....(7)}$$

Therefore, an adjustment factor γ is derived as:

$$\gamma = \frac{0.4 * (\#\ of\ snowflakes\ actually\ counted\ in\ scan\ area\ of\ single\ camera)}{\#\ of\ mached\ snowflakes\ in\ virtual\ measuring\ area} \ldots\ldots\ldots(8)$$

The “re-adjusted” concentration in each size channel ($N(D_i)$) is defined as:

$$N(D_i) = \gamma * N_m(D_i) \ldots\ldots\ldots(9)$$

where γ is assumed constant ($\gamma \geq 1$). In essence, the “raw” or unadjusted SSD is simply scaled by the factor γ. The validity of this adjustment will be evaluated by comparison with SSD from the snow video imager (Newman et al. 2009) as well as determining the γ independently by comparison with the SVI as described later in Section 3.1.

2.3 Böhm’s Method

Böhm (1989) developed a general methodology for the terminal fall speed of solid hydrometeors based on the mass, the mean effective projected area (A_e; see Fig. 3, also referred to as shadow area) presented to the flow, and the smallest circumscribed area (A; circle or ellipse depending on the shape of the snow particle). Since the 2DVD can measure the fall speed of each snowflake as well as two orthogonal images (Fig. 1), we are able to compute the mass of each snowflake by inverting the Böhm equations. The assumption is that A_e which is the projected area in a plane normal to the flow, is approximately equal to the area from the side or front views (measured by the 2DVD) for irregular shaped particles. This assumption has been evaluated as being ‘reasonable’ by Szyrmer and Zawadzki (2010) who use the HVSD which gives the side view only. We first compute the Reynolds number (Re) from fall speed (V_f) and viscosity (η) as:

$$Re = \frac{2 * \rho_a * V_f}{\eta}\left(\frac{A}{\pi}\right)^{\frac{1}{2}} \quad \text{.........} \ (10a)$$

where the characteristic dimension is the 'area' diameter (A being the area of the smallest circumscribed ellipse or circle that completely encloses the particle image). The η and air density (ρ_a) are computed from temperature, air pressure and humidity. Next, we compute the Davies number (X) from Re as:

$$X = \left\{\frac{\left[\left(\frac{Re}{8.5}\right)^{\frac{1}{2}} + 1\right]^2 - 1}{0.1519}\right\}^2 \quad \text{..........}(10b)$$

Finally the mass of the snowflake is computed as:

$$m = \frac{\pi * \eta^2 * X}{8 * g * \rho_a}\left(\frac{A_e}{A}\right)^{1/4} \quad \text{..........}(10c)$$

where g is the acceleration due to gravity. The ratio (A_e/A) is referred to as the 'area ratio' or A_r which is ≤ 1. The MKS units are appropriate for the variables in (10). The relative error in the estimate of mass due to uncertainty in the fixed relation between X and Re, and in the estimation of A_r has been evaluated by Szyrmer and Zawadzki (2010) as between 40-50%. The propagation of error from (10a) to (10c) is complicated and the reader is referred to the aforementioned reference for details.

The calculation of the minimum circumscribed area (A) is based on the rectangle which completely encloses the particle (the rectangle width is W_r and height is H; see Fig. 1).

We first assume that, (i) A is the maximum ellipse that can be fitted inside the rectangle and compute the area ratio A_e/A which should be ≤ 1. If this ratio is greater than 1, we assume that, (ii) A is the minimum circle that can contain the rectangle. The minimum circumscribed area estimated from (i) usually tends to underestimate A whereas from (ii) tends to overestimate A. The apparent volume (VL_{app}) and apparent diameter (D_{app}) were defined earlier, thus the density (ρ) is obtained as the ratio of mass (m) to VL_{app} for each particle. Since our measurements are restricted to frozen ice precipitation, the density is also restricted to min[m/VL_{app} 0.917] in cgs units. The mean density is calculated for each size bin and a power law fit of the form $\rho=\alpha D_{app}^{\beta}$ is obtained for the precipitation event. Here D_{app} is in mm and ρ is in g cm^{-3}. The mass-D_{app} power law then is $m=\alpha(\pi/6)D_{app}^{\beta+3}$.

For an area sampling measurement device such as the 2DVD, the liquid equivalent snow rate (SR_m) can be computed directly as:

$$SR_m = \frac{3600}{\Delta t}\sum_{i=1}^{N}\sum_{j=1}^{M}\frac{VL_j}{A_j}; \qquad [mm\ hr^{-1}]\ \dots\dots\dots.(11),$$

where N is the number of size bins, M is the number of snowflakes in the ith size bin in Δt (typically 60 seconds), VL_j is the liquid equivalent volume of jth snowflake in mm^3 (this is the product ρVL_{app} where ρ as a function of D_{app} is given by the power law fit) and A_j is the measurement area for the jth snowflake in unit of mm^2. The adjusted snow rate is $SR = \gamma * SR_m$ where the $\gamma-$factor was defined in Section 2.2.

We use the T-matrix (Waterman 1971; Barber and Yeh 1975) method to compute the radar cross-section of each particle and the equivalent reflectivity assuming:

- Refractive index: computed by the Maxwell-Garnet (1904) mixing formula with temperature from environmental data. The particle is assumed to be a mixture of ice inclusions within an air matrix with effective density ρ as a function of D_{app} as given by the 2DVD-derived power law fit
- Orientation: the zenith angle is Gaussian with zero mean and 45° standard deviation; the azimuthal angle is uniformly distributed in [0 π]
- Particle Size Distribution: as in Section 2.2 which defines $N(D)=\gamma*N_m(D)$
- Particle shape: oblate spheroid with volume = VL_{app} and axis ratio = 0.8

3. Experimental Data from LPVEx

The Light Precipitation Validation Experiment (LPVEx) was held in the Fall of 2010 in the area surrounding Helsinki, Finland as a collaborative project between the Finnish Meteorological Institute (FMI), University of Helsinki and the NASA Ground Validation program (Petersen et al. 2011). While the experiment had multiple objectives and extensive suite of instruments, the focus herein is on snow measurements made at the Järvenpää site with the 2D-video disdrometer; this site also had the Precipitation Occurrence Sensor System (POSS; Sheppard and Joe 2008), the Snow Video Imager (SVI; Newman et al. 2009) and an OTT-PLUVIO2 gauge with Tretyakov and Alter shields (Ianza et al. 2006; Rasmussen et al. 2012). Three C-band polarimetric radars located at Kumpula, Vantaa and Kerava (Koskinen et al., 2011) provided for excellent coverage over the Järvenpää site as well as over the network of six FMI snow gauges. Fig. 4 shows the location of the 3 radars, the Järvenpää site and the gauge network. Briefly, the three radars are nearly identical with 1° beams and using simultaneous H-V polarization on transmit and simultaneous reception of the H and V polarized back-scattered signal components via two receivers. The minimum detectable Z_e is about -10 dBZ at range of 50 km. The reflectivity data from each radar covering matched areas of precipitation were used to construct the CDF of Z_e enabling accurate cross-calibration of the radars (Hirsikko et al, 2013). All the radars are Vaisala dual-polarization weather radars, a detailed description of Vantaa radar operations is presented by Saltikoff and Nevvonen, (2011).

Table 1 lists the four snow days where there was significant precipitation in Helsinki and surrounding areas. The snow events on these days were also favorable for 2DVD and other snow measuring instruments as the wind speeds were < 4 m s^{-1} at the Järvenpää site. As seen in Table 1, the 30 Dec 2010 case could be sub-divided into two snow events based on the synoptic conditions. Similarly, the first event on 12 Jan 2011 (0800-1230 UTC) could be separated from the second event that covered the period 2230-2359 UTC which further continued the next day (13 Jan) until 0500. The liquid equivalent snow accumulations (*SA*) from the OTT-PLUVIO gauge ranged from 1.5 to 4.2 mm.

3.1 Example of 2DVD processed data from 30 Dec 2010

As mentioned earlier, one of the fundamental measurements provided by the 2DVD is the fall speed, an example of which is provided in Fig. 5 from the first event on 30 Dec 2010. The instrumental error in measuring terminal fall speeds is < 4% (for fall speeds <10 m s^{-1}; Schönhuber et al. 2008). Such high accuracy is due in part to the plane distance calibration which is performed frequently and accounts for slight deviations in the plane distance depending on the location within the virtual measurement area (see Fig. 2); further the line scan frequency is quite high close to 55 kHz. Zawadzki et al. (2010) evaluated the fall speed measurement error for the HVSD which, to the best of our knowledge, does not account for plane distance deviations within the measurement area plus the line scan frequency is much lower, closer to 10 kHz. They estimated that the instrumental uncertainty for the HVSD is around 12% for fall speeds below 2 m s^{-1}. While a similar analysis has not been done for the 2DVD, the contribution of instrumental error to the fall speed is expected to be much smaller than the natural variability which is depicted by the ±1σ bars in Fig. 5. It is also evident that the commonly used power law fit for V_f versus D, while analytically convenient, does not fit the data as well as an exponential fit of the form $V_f = c[1 - d*exp(- \kappa D_{app})]$.

The snow size distribution (SSD) for the same event is shown in Fig. 6a where the distribution from 2DVD is compared with that derived from the Snow Video Imager (SVI). The γ-factor was estimated as 2.21 (Section 2b and eq. 8). Fig. 6b shows similar plot for 6 Jan. 2011 event. The agreement in the SSD is quite good given that the two instruments are based on distinctly different measurement principles and sample volumes.

As a further check on the estimation of γ *using (8)*, the unadjusted SSD from the 2DVD has been forced to match the SVI in each size bin and the resulting mean γ_{SVI} is computed as:

$$\gamma_{SVI} = \frac{1}{N}\sum_{i=1}^{N}\frac{N_{SVI}(D_i)}{N_m(D_i)} \text{..........}(12)$$

where N is the number of size bins, $N_{SVI}(D_i)$ is the SVI-measured concentration for the i^{th} bin, and the corresponding 2DVD-measured $N_m(D_i)$ is obtained as in (6). For the case shown in Fig. 3.3 the γ_{SVI} was found to be 2.46 which is in close agreement with γ = 2.21. For the other snow events listed in Table 1 the γ comparisons are given in Table 4. As noted in the introduction the SVI gives a measure of the equal-area circular diameter which is not the same as D_{app} from the 2DVD. We ignore the different estimates of D from the two instruments is so far as validation of the single camera-2DVD based γ-factor estimation is concerned. A more elaborate discussion of SVI estimation of different measures of D and related characterization of uncertainties in estimation of Z_e and SR are given in Wood et al. (2013).

The area ratio (A_r) discussed in Section 2c plays an important role in inverting Böhm's methodology to derive mass from the fall speed. Schmitt and Heymsfield (2010) comment that, "…area-dimensional and mass-dimensional relationships are rarely developed from the same dataset". Fig. 7 shows the frequency of occurrence plot (in log scale) of A_r vs. D_{app} for the same 30 Dec 2010 snow event. Also shown are the bin averaged mean and ±1σ standard deviation bars along with the power law fit

$A_r = 0.71\ D_{app}^{-0.08}$. The variability in A_r is quite large but in general agreement with Zwadzki et al. (2010) who used data from the HVSD but allowed A_r > 1. The mean fit in Fig. 7 is in good agreement with that given in Zawadzki et al; they obtain A_r=$0.75D^{-0.17}$ (but their 'D' is the maximum dimension from the side-view image). A somewhat different power law fit was obtained by Schmitt and Heymsfield (2010), who used cloud imaging probe on aircraft penetrations of ice clouds aloft (this is not surprising since our results are at the surface in heavier snowfall). Schmitt and Heymsfield obtained an exponent of −0.25 for the ARM data set (Heymsfield et al. 2004), but their coefficient was lower by a factor of 2.

The final result from Böhm's methodology is the ability to derive a mean density-D_{app} power law and Fig. 8 shows the same for the 30 Dec 2010 event. While there is large variability in density for a given D_{app} (especially evident for small particles D_{app}< 1 mm which might be related to difficulty in matching such particles from the two camera images resulting in erroneous fall speed determination); nevertheless, there is an inverse relation between density and D_{app} and the power law fit is $\rho=0.15\ D_{app}^{-0.86}$ for this event (Table 1 gives the coefficient and exponent for the other events). Plots of ρ versus D_{app} from Table 1 using the coefficient (α) and exponent (β) found herein for the four snow days are close to the mean climatological relation found by Brandes et al. (2007; α=0.178, β=-0.922) as well as Holroyd (1971; α=0.17, β=-1) and Fabry and Szyrmer (1999; α=0.15, β=-1) with the caveat that 'D' in each of the quoted references are not calculated in the same manner (see, also, Table 2 from Brandes et al. 2007). The exponent of the mass-D_{app} power law is given by 3+β; from Table 1, the latter exponent varies between 2.04 to 2.21 generally within the range obtained by Schmitt and Heymsfield (2010) based on fractal simulations of large aggregates (range between 2.1−2.2), and close to the experimentally obtained exponent of 2.2 for the ARM dataset (Heymsfield et al. 2004).

The liquid equivalent snow rate (*SR*) for the 30 Dec 2010 is calculated as given in (11) using the mean ρ-D_{app} power law fit from Table 1 for the two snow events that occurred on that day. The *SR* is adjusted by the γ factor. Fig. 9 shows the liquid equivalent snow accumulation from the 2DVD compared with the collocated OTT-PLUVIO2 gauge at the Järvenpää site. The maximum *SR* during the two snow periods occur at around 1230 and 2200 UTC. The agreement between 2DVD and gauge is very good for this event (accumulations are based on 1-min *SR* from 2DVD). From Table 1, the accumulations between the 2DVD and gauge for the other days are also in good agreement. It is difficult to estimate the accuracy of the 2DVD-derived snow rate but assuming the ρ-D_{app} is 'exact' and valid for the entire event, the dominant systematic error would be in the γ-adjustment parameter of the SSD. Otherwise, systematic error would primarily arise due to incorrect estimate of α and secondarily β.

3.2 Reflectivity and Z_e-SR power law

The reflectivity (Z_e) at C-band (frequency 5.5 GHz) is computed from 2DVD-measured 1-min averaged $N(D_{app})$ and the mean ρ-D_{app} power law fit (for the entire event), based on the assumptions listed towards the end of Section 2.3. It is well established that for Rayleigh scattering and using the Maxwell-Garnet mixing formula (ice inclusions inside an air matrix) that Z_e can be expressed as:

$$Z_e = \left(\frac{1}{\rho_{ice}}\right)^2 \frac{|K_{ice}|^2}{|K_w|^2} \int_{D_{min}}^{D_{max}} \rho_{snow}^2 D^6 N(D) dD \text{ ....(12)}$$

where $|K_{ice,w}|^2$ are the dielectric factors of solid ice and water. Since the mass of the particle is $m=\rho VL_{app}$, it follows that Z_e can be simply computed (suppressing constants) as the sum(m^2) over all the particles. Thus, the reflectivity is very sensitive to the m-D_{app} relation (or, equivalently the ρ-D_{app}) as shown by a number of previous studies (e.g., Ryzhkov et al. 1998; Matrosov 2009). Errors can arise from uncertainty in the γ–factor which scales the $N(D)$ or uncertainty in the coefficient α and less so in the exponent β. Note that the T-matrix scattering code is used to compute Z_e at C-band frequency.

Fig. 10 shows time series comparison of Z_e from 2DVD, POSS [at Järvenpää site for (a) 30 Dec 2010 event and (b) 6 Jan. 2011] and the scanning Kumpula C-band radar reflectivity data extracted over the same site (areal average over 1°X 1 km). The 2DVD and POSS reflectivities are 1-min averaged whereas the Kumpula radar data were available every 5 min. The 2DVD data are somewhat more 'noisy' as compared to POSS due mainly to sampling error (the POSS has a very large sample volume by several orders of magnitude relative to the 2DVD). The sampling error in the 2DVD measure of Z_e was evaluated by Huang et al. (2011) by using two 2DVD units located side-by-side at a site in Huntsville, AL. They estimated the sampling error for reflectivity (in dBZ units) as 1.36 dB (time window for SSD integration was 1-min). They also estimated the normalized sampling error for SR as 8.5%. The temporal correlation between the three measures of Z_e is visually quite good.

By re-sampling the 2DVD and POSS reflectivities to the Kumpula radar samples, the scatter plot of 30 December 2010 case shown in Fig. 11 is obtained. The bias between POSS and 2DVD Z_e is 0.11 dB, the standard deviation is 2.9 dB, and the correlation coefficient is 0.92. The corresponding values between Kumpula radar and 2DVD are, respectively, 0.18 dB (slight radar overestimate), 4.68 dB and 0.8. The latter standard deviation values would be even lower if the 2DVD sampling error of 1.3 dB were accounted for.

The 2DVD processing described thus far gives the time series of Z_e and SR every minute (i.e., 1-min time integration) for each of the long duration (> 4 h) events listed in Table 1. In order to realize a 'stable' Z_e-SR relation the sequential intensity filtering technique (SIFT) described by Lee and Zawadzki (2005) is used along with weighted total least-squares to estimate the coefficient and exponent of the Z_e-SR power law. The basic time window (W) selected is 1 h; the SSDs are ordered by increasing Z_e in this window; and a moving average of $M=5$ consecutively ordered SSDs is done to filter the DSDs. The same procedure is performed for the next hour of the event and so on until the entire snow duration is covered. From the filtered DSDs, the Z_e is re-computed using the appropriate ρ-D_{app} power law. To re-compute SR, eq. (11) can no longer be used, rather it is computed as:

$$SR = \frac{\pi}{6}\int \rho\left(D_{app}\right) D_{app}^{3} V_f N\left(D_{app}\right) dD_{app} \quad \text{..........(13)}$$

where $\rho = \alpha D_{app}^{\beta}$ is the mean fit, and $V_f = c - d{*}exp(-\kappa D_{app})$ is the mean fit to the measured fall speeds (see example in Fig. 5).

Fig. 12 shows the scatter plot of Z_e versus SR and the power law fit for (a) the entire 30 Dec 2010 case (i.e., inclusive of both events listed in Table 3) and (b) 6 Jan. 2011 case. Table 3 shows the Z_e-SR power law fits for the other three snow days. For reference the FMI climatological relation is $Z_e=100\ SR^2$ (Saltikoff et al., 2010) It is fairly evident that for a given Z_e, the SR from the FMI relation will exceed that predicted from Table 3 power law fits. For completeness Table 4 shows the γ-adjustment values, and the parameters [$c\ d\ \kappa$] of the V_f-D_{app} fit.

3.3 Radar-derived snow accumulations

There were three C-band polarimetric radars operating during LPVEx, being located at (see Fig. 4) Kumpula (KUM), Kerava (KER) and Vantaa (VAN). The technical specifications can be found in (Hirsikko et al, 2013; Saltikoff and Nevvonen, 2011). When radar reflectivity is used along with a Z_e-SR relation to generate, e.g., daily (liquid equivalent) snow accumulation maps, clutter and beam-blockage at low elevation angles can cause loss of signal (in the case of clutter, due to clutter filtering) which manifests as artifacts in the snow accumulation maps. To avoid this problem, Z_e data from the three radars have been composited, using maximum reflectivity factor from any of the three radars, to generate the snow accumulation map for 30 Dec 2010 as shown in Fig. 13. The peak accumulation is around 12 mm within the city of Helsinki. The solid black dots are the locations of six FMI snow gauges (Vaisalla VRG101 with Tretyakov wind shield; Lanza et al. 2006) and the OTT-PLUVIO at Järvenpää site. The numbers adjacent to the gauge locations are the measured accumulations in mm. The radar composite, of course, depicts quite clearly the spatial variability without any artifacts due to clutter or beam blockages; moreover the radar-based accumulations are in good agreement with the gauges. Fig. 14 shows the accumulation map using the climatological FMI Z_e-SR relation and it is readily apparent that, while the spatial variability is generally preserved, the magnitudes of the accumulations are overestimated relative to the gauges. In particular, the peak accumulations are now around 16 mm within the city.

To further detail the radar and gauge comparisons, hourly accumulations are compared in Fig. 15 from one gauge location (solid dot in Fig. 13 with 7.8 mm; this is the Porvoo Harabacka location). Whilst it is clear that the FMI climatological relation overestimates the hourly accumulations soon after the snow begins, the radar-based hourly accumulation agrees well with the gauge (and not just the event totals).

Fig. 16 (panel **a**) shows the scatter plot of daily gauge accumulations versus radar-based accumulations (extracted from the radar composites over the six gauge locations and the gauge at the Järvenpää site) for the 4 days using the Z_e-SR power laws from Table 3 while panel **b** shows the same except for using the fixed FMI climatological Z_e-SR relation. The significant feature is the dramatic reduction in bias resulting from using the Z_e-SR obtained from 2DVD data as listed in Table 3 as compared with the fixed FMI relation. The normalized bias and normalized standard error values are, respectively, 28% and 30.8% when Table 3 is used versus 96.6% and 66.1% for the fixed FMI relation. Note that positive bias implies radar overestimates the gauge values. The slope of a straight line trend passing through the origin is 1.2 for panel **a** versus 1.85 for panel **b**. It is reasonable to infer that the FMI gauges could have underestimated the snow amounts due to wind and type of shielding (i.e., collection efficiency < 1). Recall that the FMI gauges are Vaisala VRG101 with Tretyakov wind shields whose collection efficiency is not known as a function of wind speed. The collection efficiency (or, undercatch) is a complicated function of not only gauge/shield type and wind speed, but also the type of snow particle (dry vs. wet or unrimed vs. rimed) and particle size distribution (Thériault et al. 2012). Thus, there is considerable scatter of the collection efficiency for a given wind speed along with a systematic decrease with increasing wind speed. The latter can be estimated from Rasmussen et al. (2012; their Fig. 11) as mean collection efficiency dropping to 0.75 at wind speed of 4 ms^{-1}. If this is taken into account the bias between radar and FMI gauges seen in Fig. 16a would be further reduced.

3.4 Spatial reflectivity structure for 30 Dec 2010 and 06 January 2011 cases

So far, the reflectivity structure nor the environmental/synoptic conditions have been described for the different snow days, as the main emphasis was on the 2DVD data, its processing and product evaluation. However, it is useful to consider the reflectivity structure for the 30 Dec 2010 case (which had the most daily accumulation) and the 06 Jan 2011 case which had the least (Table 2 or Fig. 16), accompanied by very different coefficients/exponents of the Z_e-SR power laws (respectively, 210/1.63 versus 130/1.44).

On 30 Dec 2010 large scale snowfall areas from ESE (the first snowfall from 0800-1300 UTC; see Fig. 10a) and from WNW (second snowfall from 1500-2400 UTC) merged above southern Finland. These snowfall areas were associated with two low pressure systems, one centered in Eastern Europe and the main one forming NW of Scandinavia. At around 1900 UTC the two precipitation systems have merged. ADMIRARI (Battaglia et al., 2010) LWP (liquid water path) observations reached a maximum of 400 g m^{-2} at 1500 UTC. During the observations ADMIRARI was located in the backyard of Vaisala which is around 10 km north from Kumpula radar, as shown in Fig. 4. This is the time when the warm moist area from NW had arrived to the Helsinki region. During the snowfall the LWP values were ranging between 100-150 g m^{-2}. It should be noted that these are the slant LWP observations with elevation angle of 30^{o}. At the time of peak snowfall for the first event (1100-1200 UTC; see Fig. 10a) SVI images were viewed and it was observed that the main precipitation types were pristine dendritic type crystals with large aggregates composed of dendrites (~ 8 mm) with little evidence of riming (Newman, personal communication). Fig. 17 shows sample SVI images at 1120 UTC near the time of maximum Z_e (see Fig. 10a).

On 06 Jan 2011 south westerly upper level flow from Scandinavia brought warm and moist air that resulted in a light to moderate snowfall lasting from 0100 to 0800 UTC. During this period (0500-0700 UTC) the ADMIRARI showed a large amount of supercooled water with LWP values exceeding 500 g m^{-2}. Examination of SVI images between 0600-0630 showed definite indications of rimed dendrites and columnar crystals followed by rimed to heavily rimed particles (perhaps graupel). Further in time, large aggregates (~5-7 mm) appear to be rimed. Also, many smaller rimed snowflakes/crystals (Newman, personal communication). Fig. 18 shows examples of SVI images of rimed aggregates at 0620 UTC.

Fig. 19 shows the rather dramatically different reflectivity structures (at low elevation angle 0.5°) between the 30 Dec 2010 event (at 1000 UTC) and the 06 January 2011 event (at 0610 UTC). The spatial variability is much more pronounced in the 06 January case (more cellular) as compared to the more conventional spatial variability occurring on 30 Dec. The cellular feature implies weak imbedded convection is likely with more prevalent particle riming as alluded to earlier. This is supported by analysis by Lim et al. (2013) who were able to associate higher spatial variability with enhanced riming of particles. The vertical structures are also different as depicted in the RHI scans in Fig. 20 taken along the radial to the Järvenpää site Again, the 30 Dec event is much more uniform in the vertical as compared with the 06 Jan event, the latter showing more evidence of cellular structure in the vertical implying imbedded convection and enhanced riming.

Finally, in Fig. 21, the snow accumulation map for 06 Jan event is shown using the 2DVD-derived Z_e-SR power law, which can be compared with Fig. 13. The snow accumulations for this event (see, also Table 1) are much smaller compared with 30 Dec case additionally showing much more spatial variability. Note these are not daily totals but restricted to the period 0000-0900 UTC since the 2DVD stopped working at 0824 UTC on this day thereby missing another major snowfall event later on this day.

4. Summary and Conclusions

The estimation of the mean density-size and Z_e-SR power laws using 2D-video disdrometer measured fall speed, apparent diameter and snow size distribution (SSD) along with Böhm's (1989) methodology is described in some detail. A method for adjusting the concentration based on single camera data to account for loss of particles that do not satisfy the matching criteria (when 2 cameras are used) is shown to be reasonable when compared with Snow Video Imager (SVI)-based concentrations. Snow events which occurred on four days of the Light Precipitation Validation Experiment (LPVEx) were chosen based on light wind speeds (< 4 ms^{-1}) at the measurement site with liquid equivalent snow accumulations ranging from 1.5 mm to 4 mm. While there is large variability of fall speed, area ratio and derived density which is attributed to natural variability of snow type, shape and porosity, the mean density-D_{app} (or, mass-D_{app}) and Z_e-SR power laws do vary from event-to-event. The reflectivity derived from the 2DVD data is shown to be in good agreement with collocated POSS and with scanning C-band radar, while the liquid equivalent snow accumulation is shown to be in good agreement with collocated OTT-PLUVIO gauge at the measurement site. The radar-based snow accumulations using the 2DVD-derived Z_e-SR relations for the four days are in good agreement with a network of six FMI snow gauges (and the OTT-PLUVIO gauge) and outperform the accumulations derived from a climatological Z_e-SR relation used by the Finnish Meteorological Institute (FMI). The normalized bias between radar-derived and gauge accumulation is reduced from 96%

(overestimate by the FMI climatological relation) to 28% when using the Z_e-SR based on 2DVD data. The normalized standard error is also reduced significantly from 66% to 31%. While the FMI gauges were equipped with Tretyakov wind shields, undercatchment due to wind cannot be ignored and could account for underestimation of snow accumulations by 20-30% for wind speeds in the range 3-4 ms^{-1}; this would reduce the bias between radar and gauge accumulations even further.

For two of the days with widely different coefficients of the Z_e-SR power law, the reflectivity structure showed significant differences in spatial variability (both horizontal and vertical). Liquid water path estimates from radiometric data also showed significant differences between the two cases. Examination of SVI particle images at the measurement site corroborated these differences in terms of unrimed versus rimed snow particles.

In summary, the findings reported herein support the application of Böhm's (1989) methodology for deriving the mean density-size and Z_e-SR power laws using data from 2D-video disdrometer. Evaluation of radar-based snow accumulation against a network of snow gauges independently supports the latter conclusion notwithstanding the limited number of events available for analysis.

Acknowledgements. Two of the authors VNB and GJH acknowledge support from NASA grants NNX10AJ11G and NNX11AK32G. DM acknowledges support from Academy of Finland grant 263333. WAP and LB acknowledge support from NASA GPM Flight Project and Dr. Ramesh Kakar, Program Manager for PMM. The authors also acknowledge Dr. Andrew Newman of NCAR for assistance in visual classification of SVI snow images for two of the events. The SVI and POSS were installed by Peter Rodriguez of Environment Canada.

References

Barber, P. and Yeh, C., 1975: Scattering of Electromagnetic Waves by Arbitrarily Shaped Dielectric Bodies., *Appl. Optics*, **14**, pp. 2684-2872.

Barthazy, E., Göke, S., Schefold, R. and Högl, D., 2004: An optical array instrument for shape and fall velocity measurements of hydrometeors., *J. Atmos. Oceanic Technol.*, **21**, pp. 1400-1416.

Battaglia, A., Saavedra, P., Rose, T. and Simmer, C., 2010: Characterization of Precipitating Clouds by Ground-Based Measurements with the Triple-Frequency Polarized Microwave Radiometer ADMIRARI., *J. Appl. Meteor. Climatol.*, **49**, pp. 394–414.

Böhm, H.P., 1989: A general equation for the terminal fall speed of solid hydrometeors., *J. Atmos. Sci.*, **46**, pp. 2419-2427.

Brandes, E. A., Ikeda, K., Zhang, G., Schönhuber, M. and Rasmussen, R. M., 2007: A statistical and physical description of hydrometeor distributions in Colorado snowstorms using a video disdrometer., *J. Appl. Meteor. Climatol.*, **46**, pp. 634-650.

Brandes, E. A., Ikeda, K. and Thompson, G., 2008: Aggregate terminal velocity/temperature relations, J*. Appl. Meteor. Climatol.*, **47**, pp. 2729–2736.

Fabry, F., and Szyrmer, W., 1999: Modeling of the melting layer. Part II: Electromagnetic. *J. Atmos. Sci.*, **56**, pp. 3593–3600.

Fujiyoshi, Y., Endoh, T., Yamada, T., Tsuboki, K., Tachibana, Y. and Wakahama, G., 1990: Determination of a Z-R relationship for snowfall using a radar and high sensitivity snow gauges, *J. Appl. Meteor.*, **29**, pp. 147–152.

Garrett, T. J., Fallgatter, C., Shkurko, K. and Howlett, D., 2012: Fallspeed measurement and high-resolution multi-angle photography of hydrometeors in freefall., *Atmos. Meas. Tech. Discuss.*, **5**, pp. 4827−4850.

Hanesch, M., 1999: Fall Velocity and Shape of Snowflake., Ph. D dissertation, *Swiss Federal Institute of Technology*., [Available online at http://www.distrometer.at/newReferences.html]

Heymsfield, A. J., Bansemer, A., Schmitt, C., Twohy, C. and Poellot, M. R., 2004: Effective Ice Particle Densities Derived from Aircraft Data. *J. Atmos. Sci.*, **61**, pp. 982–1003.

Heymsfield, A. J. and Westbrook, C. D., 2010: Advances in the Estimation of Ice Particle Fall Speeds Using Laboratory and Field Measurements., *J. Atmos. Sci.*, **67**, pp. 2469–2482.

Hirsikko, A., O'Connor, E., Komppula, M., Korhonen, K., Pfuller, A., Giannakaki, E., Wood, C. R., Bauer-Pfundstein, M., Poikonen, A., Karppinen, T., Lonka, H., Kurri, H., Heinonen, J., Moisseev, D., Asmi, E., Aaltonen, V., Nordbo, A., Rodriguez, E., Lihavainen, H., Laaksonen, A., Lehtinen, K., Laurila, T., Petaja, T., Kulmala, M. and Viisanen, Y., 2013: Observing Wind, Aerosol Particles, Cloud and Precipitation: Finland's New Ground-based Remote-sensing Network. *Atmospheric Measurement Techniques Discussions*, **6**, pp. 7251-7313.

Hogan, R. J., Tian, L., Brown, P. R. A., Westbrook, C. D., Heymsfield, A. J. and J. Eastment, J. D., 2012: Radar Scattering from Ice Aggregates Using the Horizontally Aligned Oblate Spheroid Approximation. *J. Appl. Meteor. Climatol.*, **51**, pp. 655–671.

Holroyd, E. W., III, 1971: The meso- and microscale structure of Great Lakes snowstorm bands: A synthesis of ground measurements, radar data, and satellite observations. Ph.D. dissertation, *University at Albany, State University of New York*, p148.

Huang, G., Bringi, V. N., Cifelli, R., Hudak, D. and Petersen, W. A., 2010: A Methodology to Derive Radar Reflectivity–Liquid Equivalent Snow Rate Relations Using C-Band Radar and a 2D Video Disdrometer., *J. Atmos. Oceanic Technol.*, **27**, pp. 637-651.

Huang, G., Bringi, V. N., Petersen, W. A., Carey, L., Schultz, C. J. and Gatlin, P. N., 2011: Case Studies of Winter Precipitation Events Using 2D-Video Disdrometers and C-Band Radar., *35rd Conf. on Radar Meteorology*, Pittsburgh, PA., Amer. Meteor.l Soc., September 26-30., P13.203. [Available online at https://ams.confex.com/ams/35Radar/webprogram/Paper191883.html]

Koskinen, J., Poutiainen, J., Schultz, D., Joffre, S., Koistinen, J., Saltikoff, E., Gregow, E., Turtiainen, H., Dabberdt, W., Pohjola, H., Ruotsalainen, R., Kuitunen, T., Järvi, L., Vesala, T., Karppinen, A., Moisseev, D., Göke, S., Pylkkö, P., Hyvärinen, O., Kotro, J., Damski, J., Nurmi, P., Kukkonen, J., Viisanen, Y. and Kulmala, M., 2011: The Helsinki Testbed: A mesoscale measurement, research and service platform. *Bull. Amer. Meteor. Soc.*, **93 (3)**, pp. 325-342.

Kruger, A. and Krajewski, W. F., 2002: Two-dimensional video disdrometer: A description, *J. Atmos. Oceanic Technol.*, **19**, pp. 602-617.

Lanza, L., M. Leroy, C. Alexandropoulos, L. Stagi and W. Wauben, 2006: WMO laboratory intercomparison of rainfall intensity gauges. Instruments and Observing Methods Report No. 84, WMO/TD-No. 1304, WMO Geneva.

Lee, G. and Zawadzki, I., 2005: variability of Drop Size Distributions: Noise and Noise Filtering in Disdrometric data., *J. Appl. Meteor.*, **44**, pp. 634–652.

Lim, S., Moisseev, D., Chandrasekar, V. and Lee, D.-R., 2013: Classification and Quantification of Snow Based on Spatial Variability of Radar Reflectivity. *J. Meteo. Soc. Japan.*, **91**, pp. 763-774.

Mason, B. J., 2010: The Physics of Clouds., *Oxford University Press.*

Matrosov, S. Y., Campbell,C., Kingsmill, D. and Sukovich, E., 2009: Assessing Snowfall Rates from X-Band Radar Reflectivity Measurements. *J. Atmos. Oceanic Technol.*, **26**, pp. 2324–2339.

Maxwell-Garnet, J.C., 1904: Colors in Metal Glasses and in Metallic Films., *Phil. Trans. Roy. Soc.*, **A203**, pp. 385-420.

Mitchell, D. L., 1996: Use of Mass- and Area-dimensional Power Laws for Determining Precipitation Particle Terminal Velocities, *J. Atmos. Sci.*, **53**, pp. 1710–1723.

Newman, A. J., Kucera, P. A. and Bliven, L. F., 2009: Presenting the Snowflake Video Imager (SVI), *J. Atmos. Ocean. Technol.*, **26**, pp. 167–179, 2009.

Petersen, W. A., L'Ecuyer, T. and Moisseev, D., 2011: The NASA CloudSat/GPM Light Precipitation Validation Experiment (LPVEx), *The Earth Observer*, **23**, Issue 4.

Pruppacher, H. R. and Klett, J. D., 2010: Microphysics of Clouds and Precipitation. (Second revised and expanded edition), *Series: Atmospheric and Oceanographic Sciences Library*, **18**, Springer.

Rasmussen R. and 14 co-authors, 2012: How Well are We Measuring Snow, *Bull. Amer. Met. Soc.*, **93**, pp 811-829.

Ryzhkov, A. V., Zrnić, D. S. and Gordon, B. A., 1998: Polarimetric Method for Ice Water Content Determination. *J. Appl. Meteor.*, **37**, pp. 125–134.

Saltikoff, E., Huuskonen, A., Hohti, H., Koistinen, J. and Järvinen, H., 2010: Quality Assurance in the FMI Doppler Weather Radar Network., *Boreal Environ. Res.*, **15**, pp. 579–594

Saltikoff, E., and Nevvonen, L. 2011: First Experiences of the Operational Use of A Dual-polarisation Weather Radar in Finland., *Meteor. Zeitschrift*, **20**, pp. 323-333.

Schmitt, C. G. and Heymsfield, A. J. 2010: The Dimensional Characteristics of Ice Crystal Aggregates from Fractal Geometry., *J. Atmos. Sci.*, **67**, pp. 1605-1616.

Schönhuber, M., Urban, H. E., Randeu, W. L. and Poiares Baptista, J. P. V., 2000: Empirical Relationships between Shape, Water Content and Fall Velocity of

Snowflakes, *ESA SP-444 Proceedings*, Millennium Conference on Antennas & Propagation, April 9-14, 2000, Davos, Switzerland.

Schönhuber, M., Lammer, G. and Randeu, W. L., 2008: The 2D-video-distrometer, Chapter 1 in *Precipitation: Advances in Measurement, Estimation and Prediction*. Michaelides, Silas. (Ed.), Springer, ISBN: 978-3-540-77654-3.

Sekhon R. S., and Srivastava, R. C., 1970: Snow size spectra and radar reflectivity. *J. Atmos. Sci.*, **27**, pp. 299–307.

Sheppard, B. E. and Joe, P. I., 2008: Performance of the Precipitation Occurrence Sensor System as a Precipitation Gauge., *J. Atmos. Oceanic Technol.*, **25**, pp. 196-212.

Szyrmer, W. and Zawadzki, I., 2010: Snow Studies. Part II: Average Relationship between Mass of Snowflakes and Their Terminal Fall Velocity. *J. Atmos. Sci.*, **67**, pp. 3319–3335.

Thériault, J. M., Rasmussen, R., Ikeda, K. and Landolt, S., 2012: Dependence of snow gauge collection efficiency on snowflake characteristics, *J. Appl. Meteor. Climatol.*, **51**, pp. 745-762.

Waterman, P. C., 1971: Symmetry, Unitarity, and Geometry in Electromagnetic Scattering., *Phys. Rev.*, **D 3**, pp. 825-839.

Wood, N. B., L'Ecuyer, T. S., Bliven, F. L. and Stephens, G. L., 2013: Characterization of video disdrometer uncertainties and impacts on estimates of snowfall rate and radar reflectivity. *Atmos. Meas. Tech.*, **6**, pp. 3635-3648.

Zawadzki, I., Jung, E. and Lee, G., 2010: Snow Studies. Part I: A Study of Natural Variability of Snow Terminal Velocity., *J. Atmos. Sci.*, **67**, pp. 1591-1604.

Zhang, G., Luchs, S., Ryzhkov, A., Xue, M., Ryzhkova, L. and Cao, Q., 2011: Winter Precipitation Microphysics Characterized by Polarimetric Radar and Video Disdrometer Observations in Central Oklahoma. *J. Appl. Meteor. Climatol.*, **50**, pp. 1558–1570.

List of Figures

Fig 1: Front- and side-view images of a snow flake from the 2DVD. The maximum ‘size’ is approximately 16 mm in the side view (Camera B); from Huang et al. (2010).

Fig. 2: Illustrating the measurement principle of the 2D-Video disdrometer (from Kruger and Krajewski 2002; Schönhuber et al. 2008). Note that the virtual measuring area is different (100 cm^2) relative to the single camera measuring area (250 cm^2).

Fig. 3: An example to show the shadow area (A_e) and the smallest circumscribed area area (A); from Böhm (1989).

FIG. 4: The map shows the location of 3 C-Band radars (KUM, VAN and KER), the Järvenpää site and other 6 FMI gauges used in this paper. Note that the OTT-PLUVIO gauge and 2DVD are sited at Jävenpää.

FIG. 5: Example of 2DVD-derived fall speeds versus apparent diameter for snow event from 30 Dec 2010 dominated by snow aggregates. For each size bin the mean and ±1σ standard deviation of the fall speed are shown. The exponential fit to the mean values of the form $V_f = 1.12\text{-}1.31{*}exp(-1.42\ D_{app})$ where D_{app} is in mm and V_f in m s^{-1} is also shown.

Fig. 6: Particle (snow) size distributions from the 2DVD and from the snow video imager (SVI) for **(a)** 30 Dec 2010 first snow event with γ equal to 2.21 **(b)** 6 Jan. 2011 event with γ equal to 2.55.

Fig. 7: Frequency of occurrence (in color log scale) of A_r vs. D_{app} for 30 Dec 2010 snow event; also shown are the bin averaged mean and ±1σ standard deviation bars along with the power law A_r–D_{app} fit.

Fig. 8: Density versus D_{app} (mean and ±1σ) along with mean ρ–D_{app} power law fit for the 30 Dec 2010 event.

Fig. 9: Liquid equivalent snow accumulation for 30 Dec 2010 comparing 2DVD-derived accumulations against collocated OTT-PLUVIO2 gauge.

Fig. 10: Time series comparison of reflectivity from 2DVD, POSS and scanning Kumpula radar for **(a)** 30 Dec 2010 event and **(b)** 6 Jan. 2011.

Fig. 11: Scatter plot of 2DVD or POSS reflectivity (Y-axis) versus Kumpula radar reflectivity (X-axis) extracted over Järvenpää site for 30 Dec 2010 event.

Fig. 12: Z_e versus *SR* scatterplot using SIFT method for (a) 30 Dec 2010 case and (b) 6 Jan. 2011. The power law fit using weighted total least squares is also shown.

Fig. 13: Snow accumulation map for 30 Dec 2010 (entire day) using Z_e-*SR* power law in Table 3. Reflectivity data from three radars have been composited. The solid black dots are locations of 6 FMI snow gauges and the numbers adjacent are the snow gauge measurements of liquid equivalent snow accumulation in mm.

Fig. 14: As in Fig. 13 except the FMI climatological $Z_e=100*SR^2$ is used.

Fig. 15: Comparison of hourly accumulations at the Porvoo Harabacka site using FMI gauge.

Fig. 16: Scatter plots of daily gauge accumulations from the seven FMI snow gauges versus radar-based daily accumulations using (top panel **a**) daily Z_e-*SR* relations from Table 3 and (bottom panel **b**) using fixed FMI climatological Z_e-*SR* relation. Data from the 4 snow days are color-coded.

Fig. 17: Example of SVI images of large aggregates at 1120 UTC on 30 Dec 2010 at Järvenpää site (also close to time of peak reflectivity, see Fig. 10a).

Fig. 18: Example of SVI images of large rimed aggregates at 0620 UTC on 06 Jan 2011 at Järvenpää site.

Fig. 19: Spatial variability of reflectivity (left panel) for 30 Dec 2010 and, (right panel) for 06 Jan cases.

Fig. 20: RHI scan data from Kumpula radar along the radial to the Järvenpää site (top panel) 30 Dec 2010 at 1053 UTC, and (bottom panel) 06 Jan 2011 at 0603 UTC.

Fig. 21: As in Fig. 13 except for 06 Jan 2011 event (0000-0900 UTC only) using 2DVD-derived Z_e-SR relation.

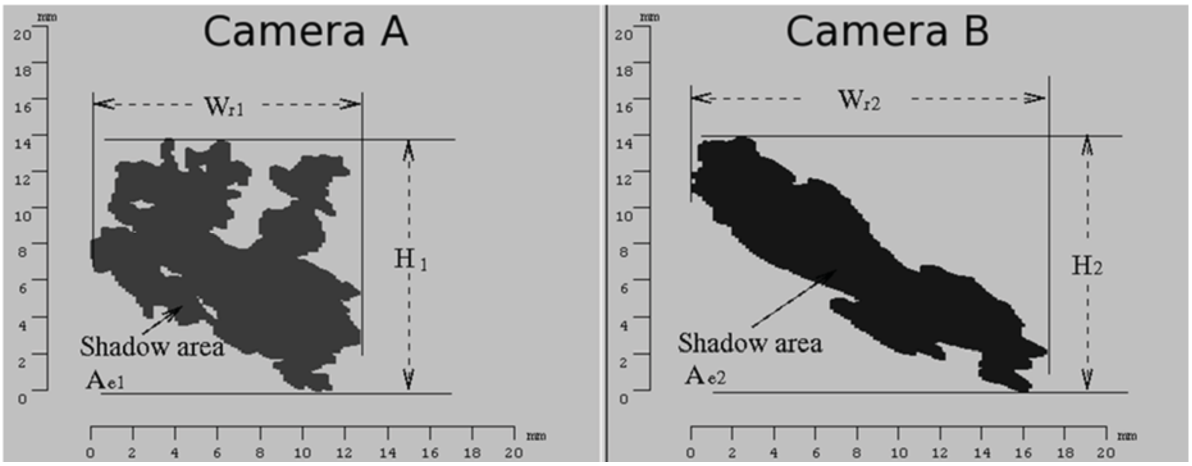

Fig. 1: Front- and side-view images of a snow flake from the 2DVD. The maximum 'size' is approximately 16 mm in the side view (Camera B); from Huang et al. (2010).

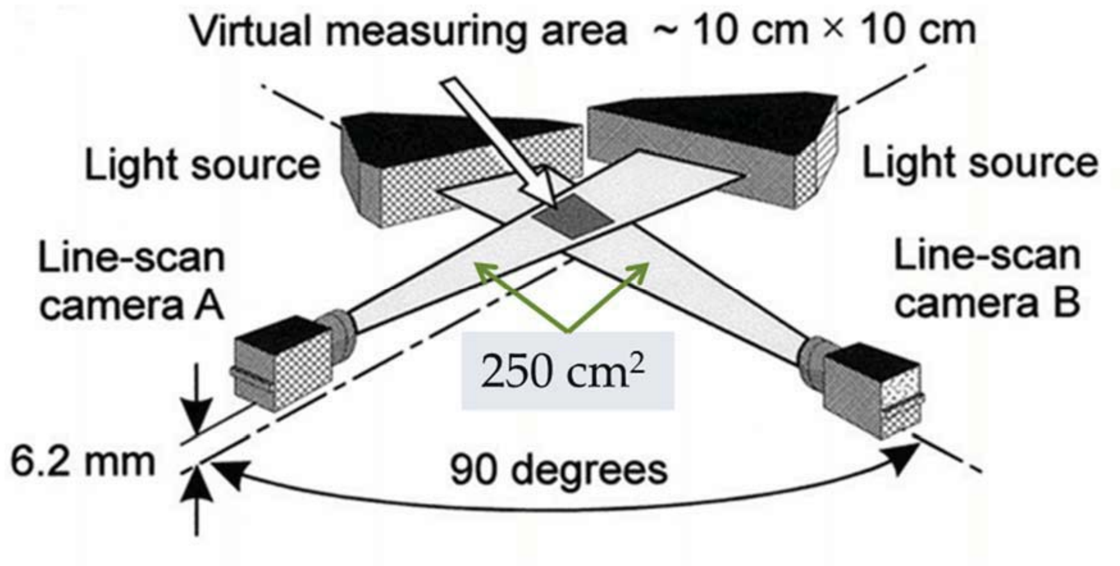

Fig. 2: Illustrating the measurement principle of the 2D-Video disdrometer (from Kruger and Krajewski 2002; Schönhuber et al. 2008). Note that the virtual measuring area is different (100 cm^2) relative to the single camera measuring area (250 cm^2).

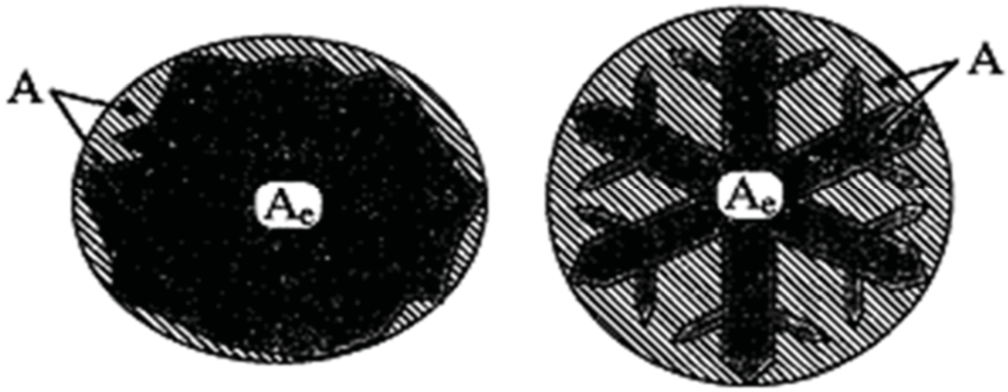

Fig. 3: An example to show the shadow area (A_e) and the smallest circumscribed area area (A); from Böhm (1989).

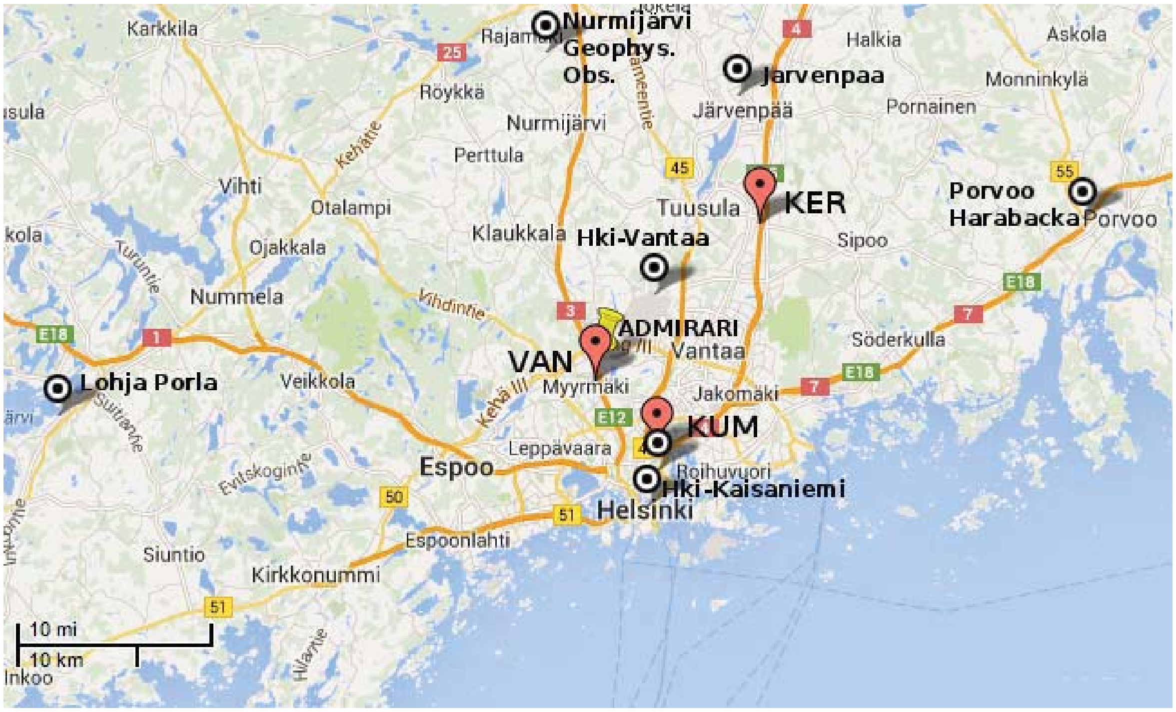

Fig. 4: The map shows the location of 3 C-Band radars (KUM, VAN and KER), the Järvenpää site and other 6 FMI gauges used in this paper. Note that the OTT-PLUVIO gauge and 2DVD are sited at Jävenpää.

819

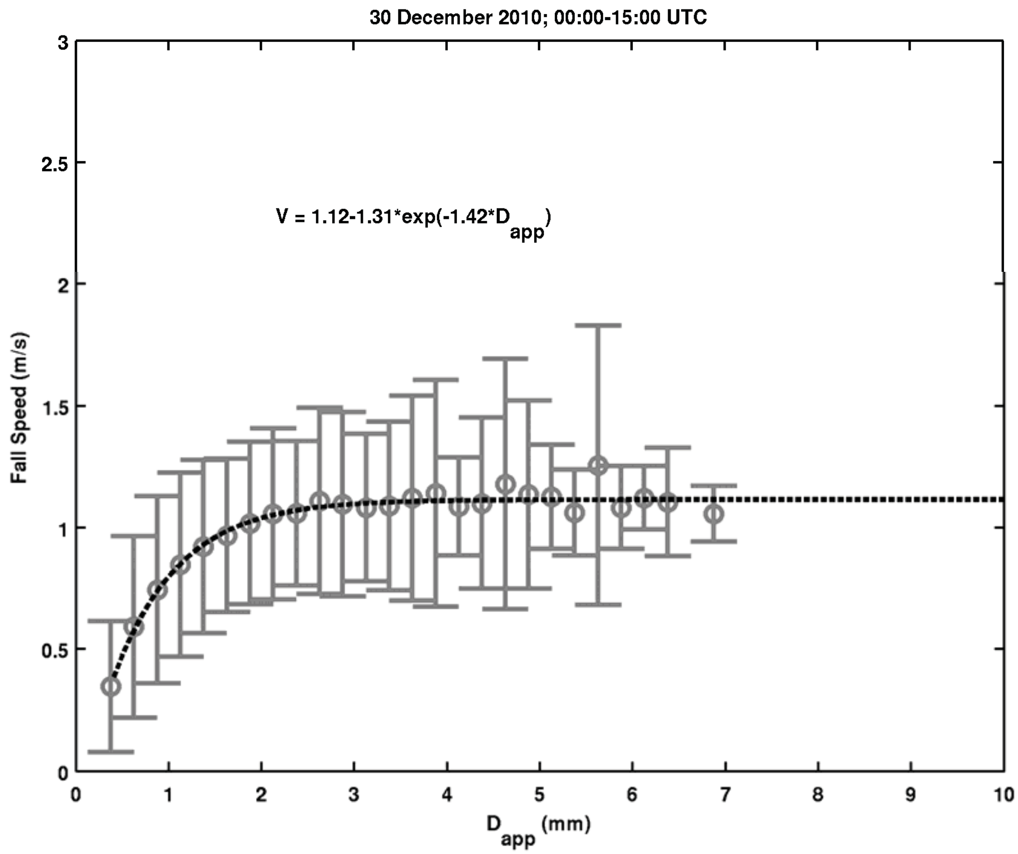

*Fig. 5: Example of 2DVD-derived fall speeds versus apparent diameter for snow event from 30 Dec 2010 dominated by snow aggregates (00:00-15:00 UTC). For each size bin the mean and ±1σ standard deviation of the fall speed are shown. The exponential fit to the mean values of the form V_f = 1.12-1.31*exp(-1.42 D_{app}) where D_{app} is in mm and V_f in m s^{-1} is also shown.*

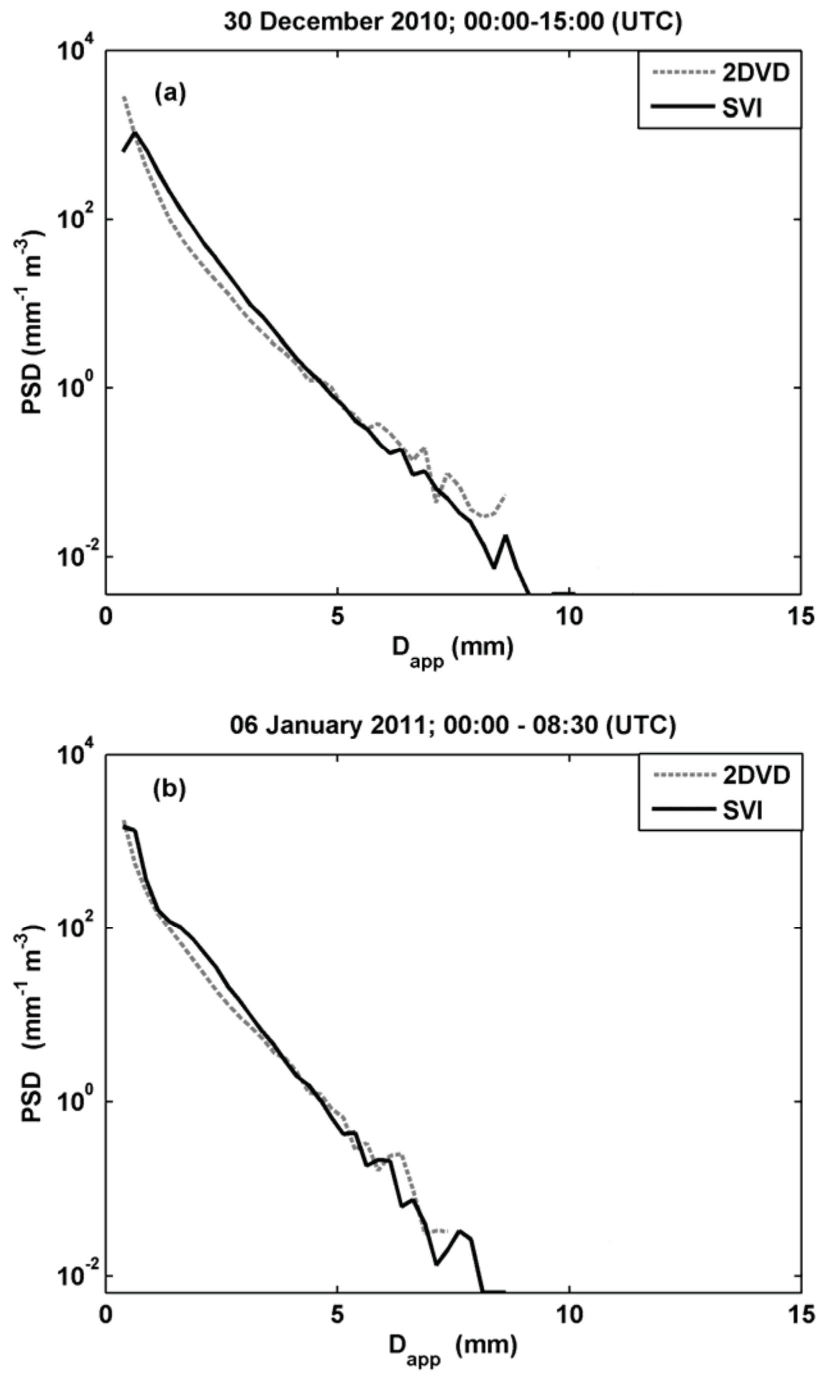

*Fig. 6: Particle (snow) size distributions from the 2DVD and from the snow video imager (SVI) for **(a)** 30 Dec 2010 first snow event with γ equal to 2.21 **(b)** 6 Jan. 2011 event with γ equal to 2.55.*

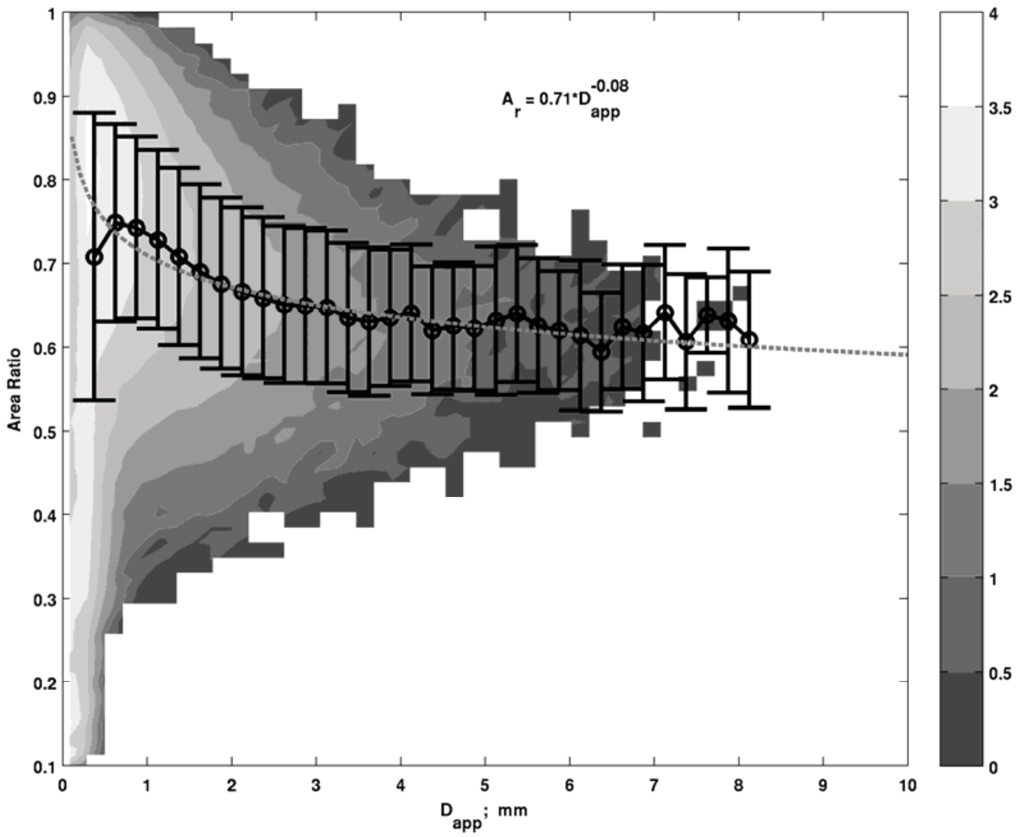

Fig. 7: Frequency of occurrence (in log scale) of A_r vs. D_{app} for 30 Dec 2010 snow event; also shown are the bin averaged mean and $\pm 1\sigma$ standard deviation bars along with the power law A_r–D_{app} fit.

823

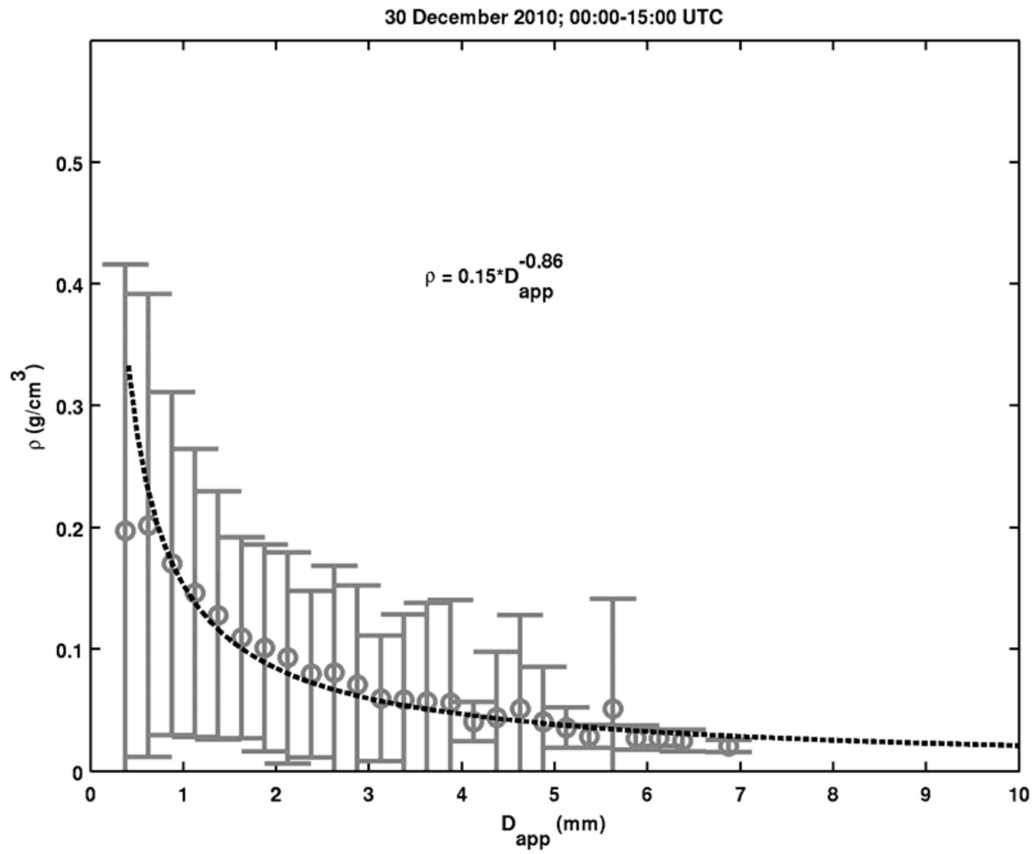

Fig. 8: Density versus D_{app} (mean and ±1σ) along with mean ρ–D_{app} power law fit for the 30 Dec 2010 event.

824

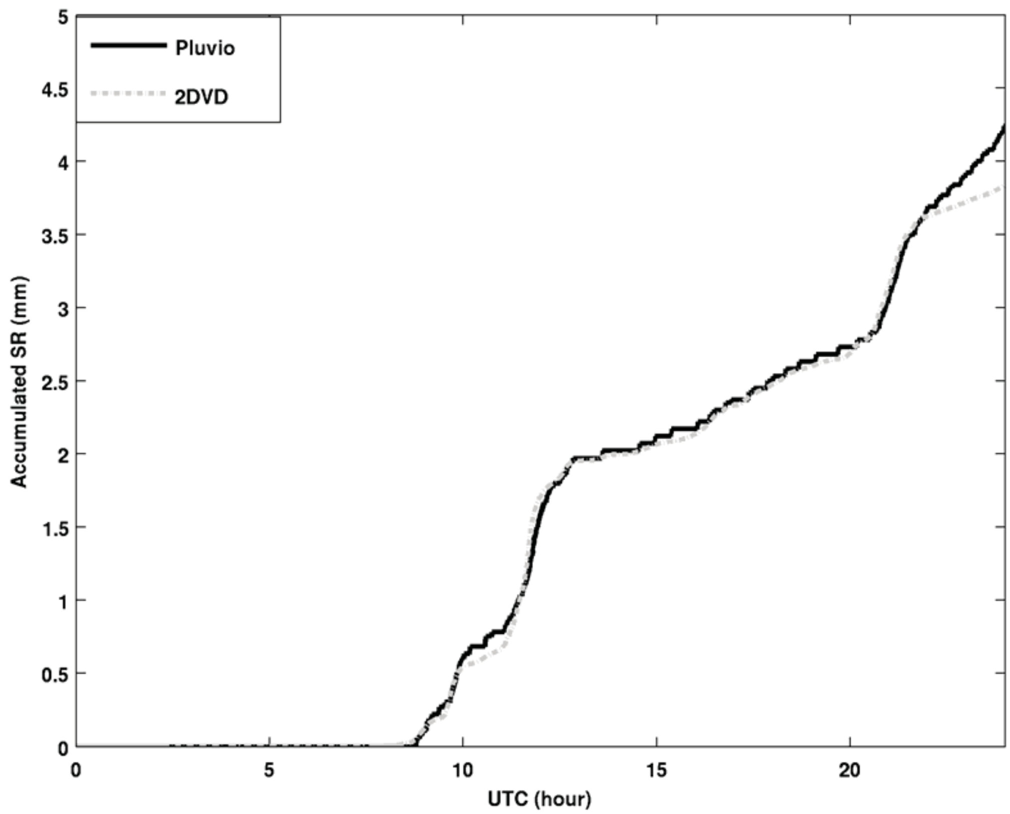

Fig. 9: Liquid equivalent snow accumulation for 30 Dec 2010 comparing 2DVD-derived accumulations against collocated OTT-PLUVIO2 gauge.

825

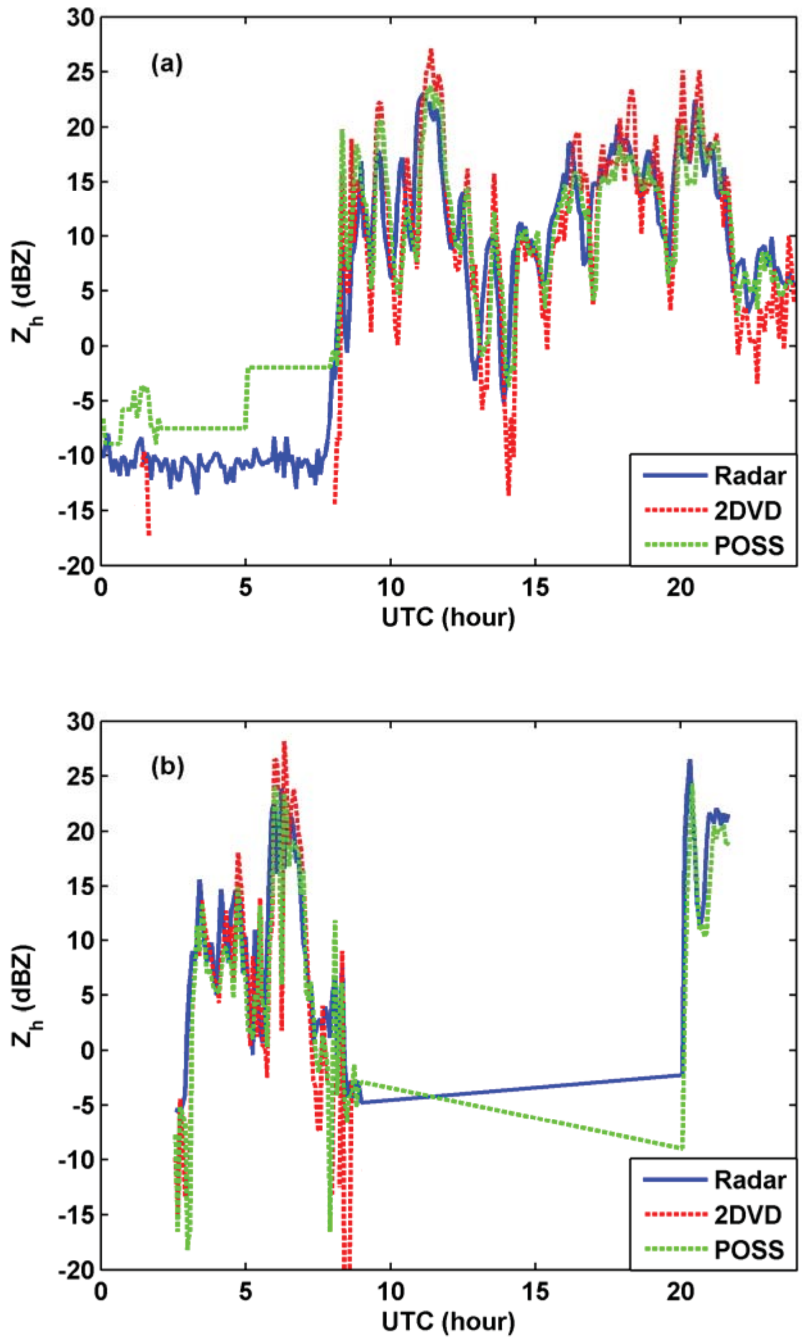

*Fig. 10: Time series comparison of reflectivity from 2DVD, POSS and scanning Kumpula radar for **(a)** 30 Dec 2010 event and **(b)** 6 Jan. 2011.*

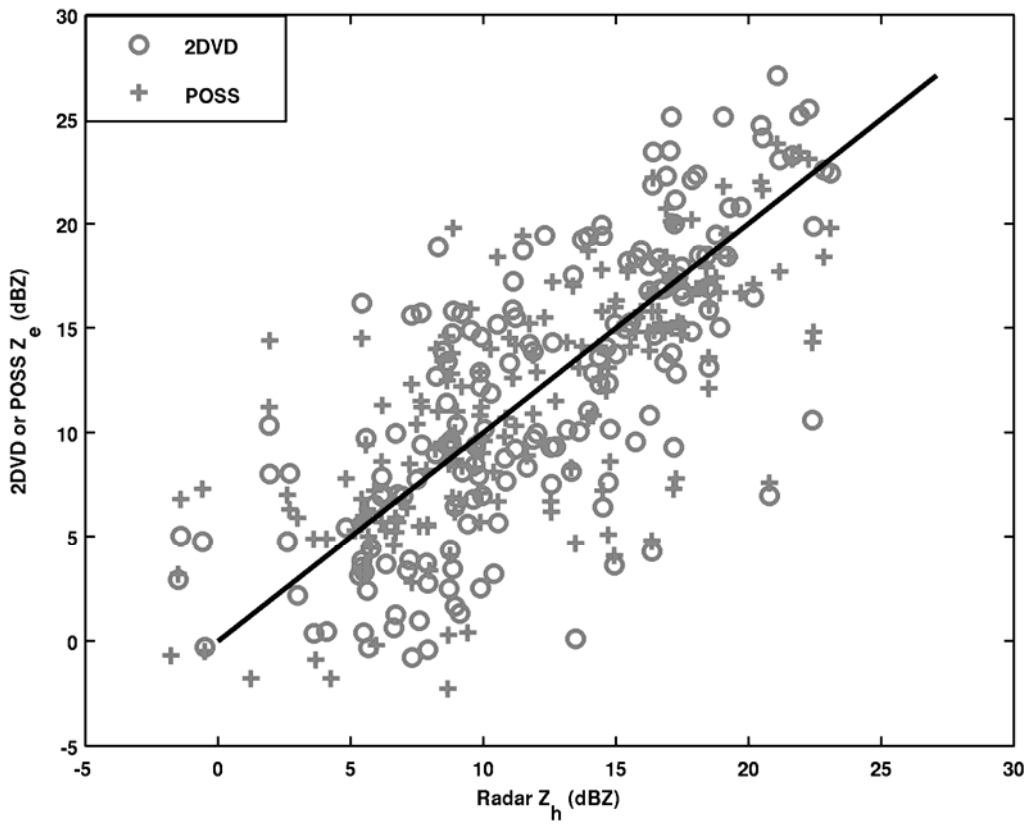

Fig. 11: Scatter plot of 2DVD or POSS reflectivity (Y-axis) versus Kumpula radar reflectivity (X-axis) extracted over Järvenpää site for 30 Dec 2010 event.

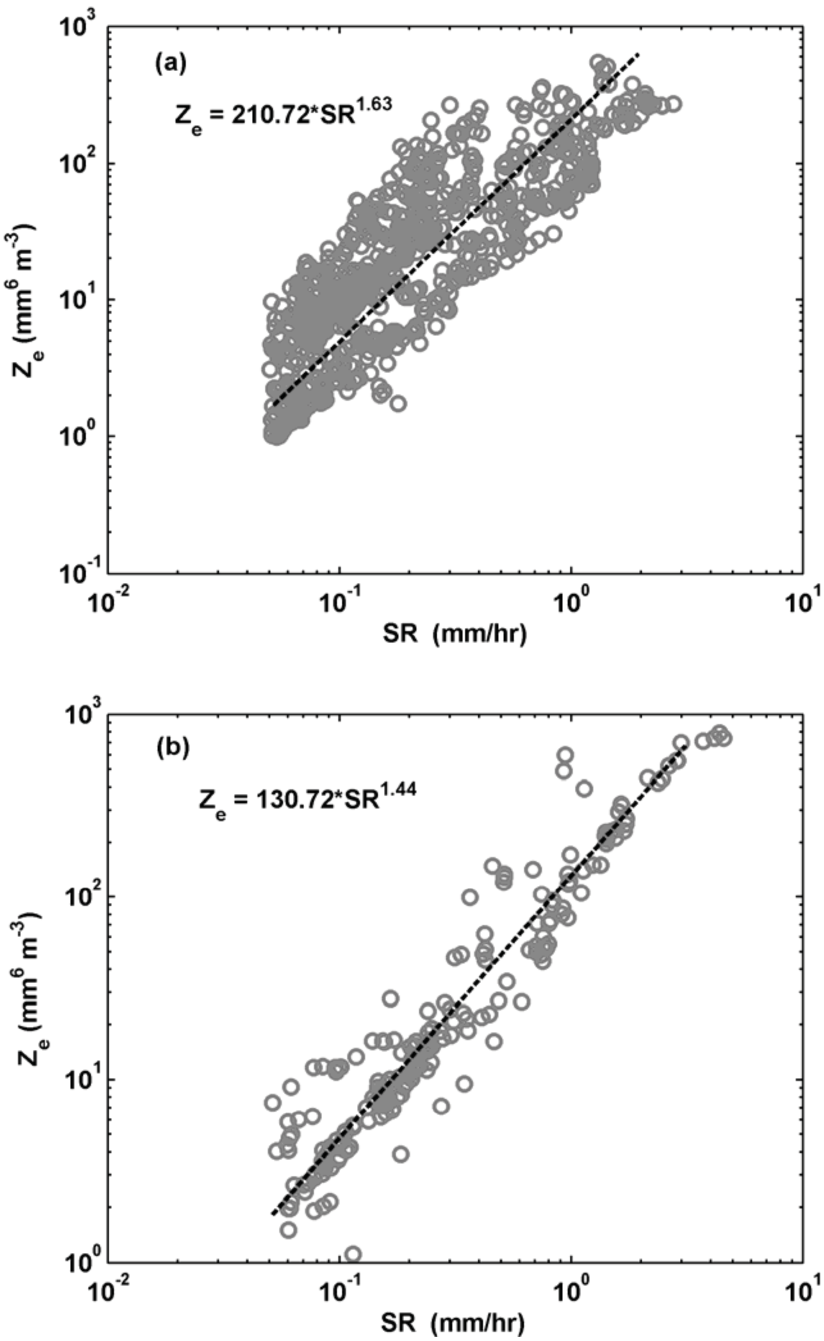

*Fig. 12: Z_e versus SR scatterplot using SIFT method for **(a)** 30 Dec 2010 case and **(b)** 6 Jan. 2011. The power law fit using weighted total least squares is also shown.*

830

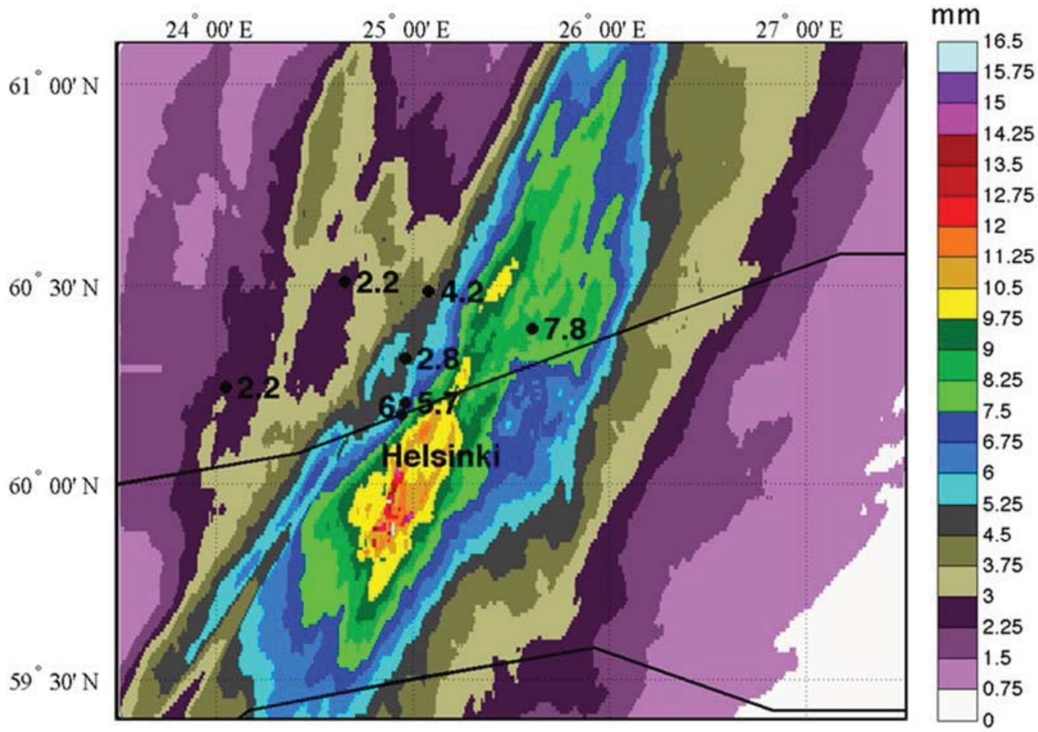

Fig. 13: Snow accumulation map for 30 Dec 2010 (entire day) using Z_e-SR power law in Table 3. Reflectivity data from three radars have been composited. The solid black dots are locations of 6 FMI snow gauges and the numbers adjacent are the snow gauge measurements of liquid equivalent snow accumulation in mm.

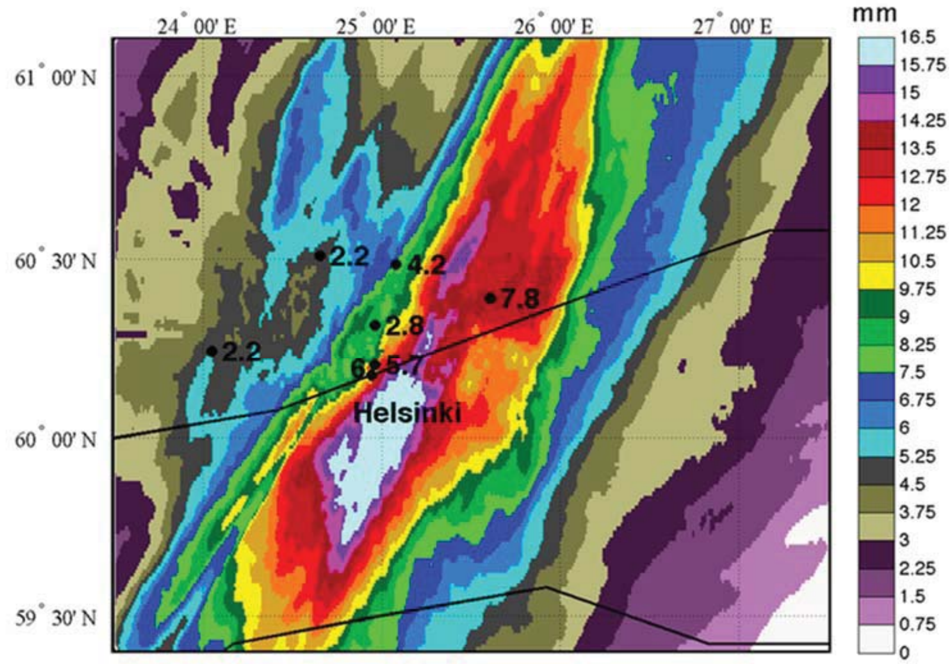

*FIG. 14: As in Fig. 13 except the FMI climatological Z_e=100*SR^2 is used.*

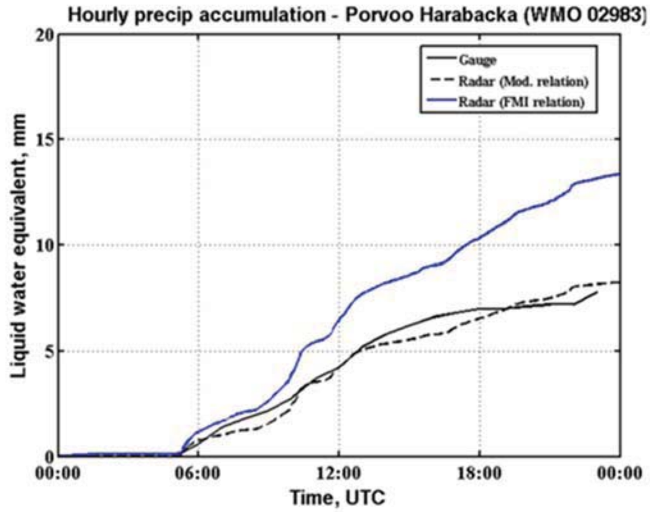

Fig. 15: Comparison of hourly accumulations at the Porvoo Harabacka site using FMI gauge.

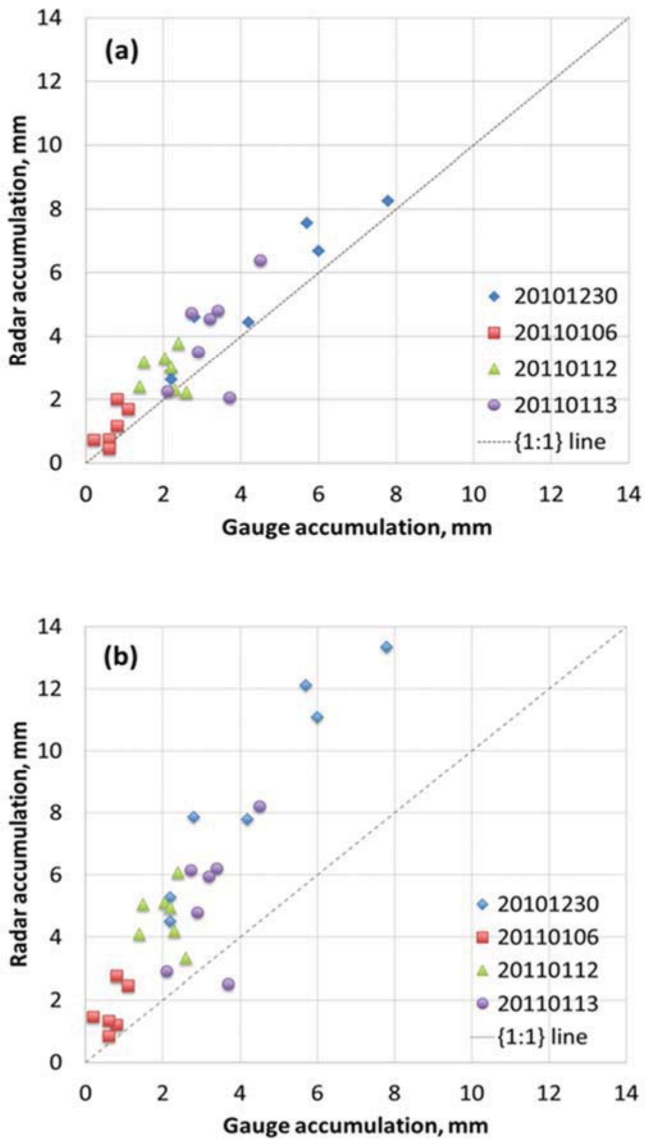

*Fig. 16: Scatter plots of daily gauge accumulations from the seven FMI snow gauges versus radar-based daily accumulations using (top panel **a**) daily Z_e-SR relations from Table 3 and (bottom panel **b**) using fixed FMI climatological Z_e-SR relation. Data from the 4 snow days are color-coded.*

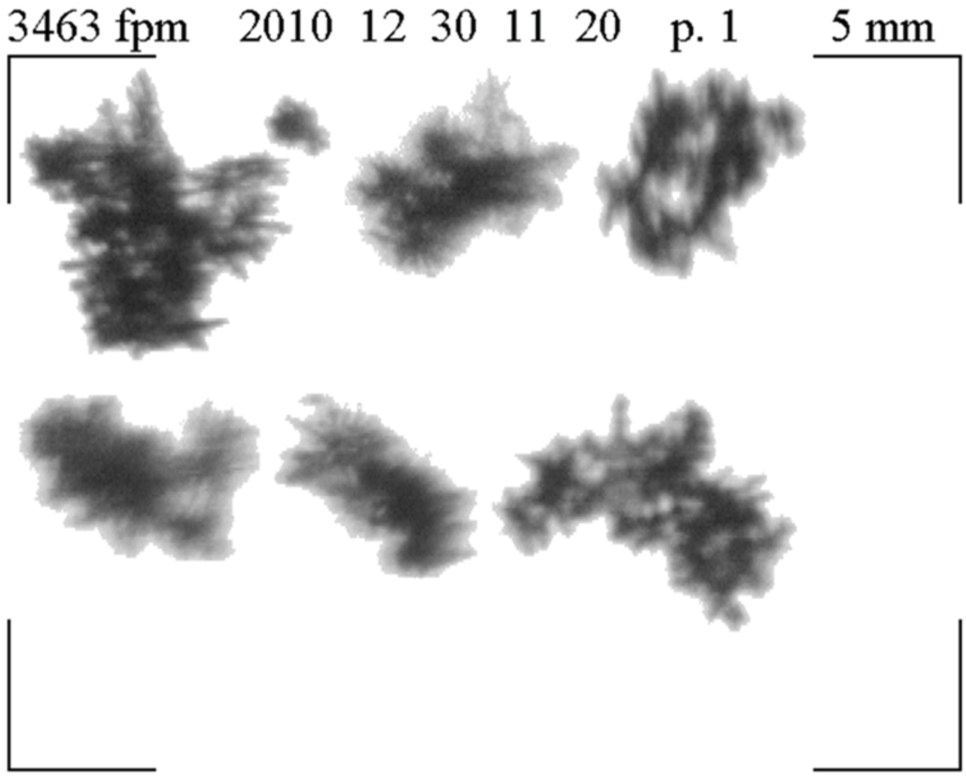

Fig. 17: Example of SVI images of large aggregates at 1120 UTC on 30 Dec 2010 at Järvenpää site (also close to time of peak reflectivity, see Fig. 10a).

835

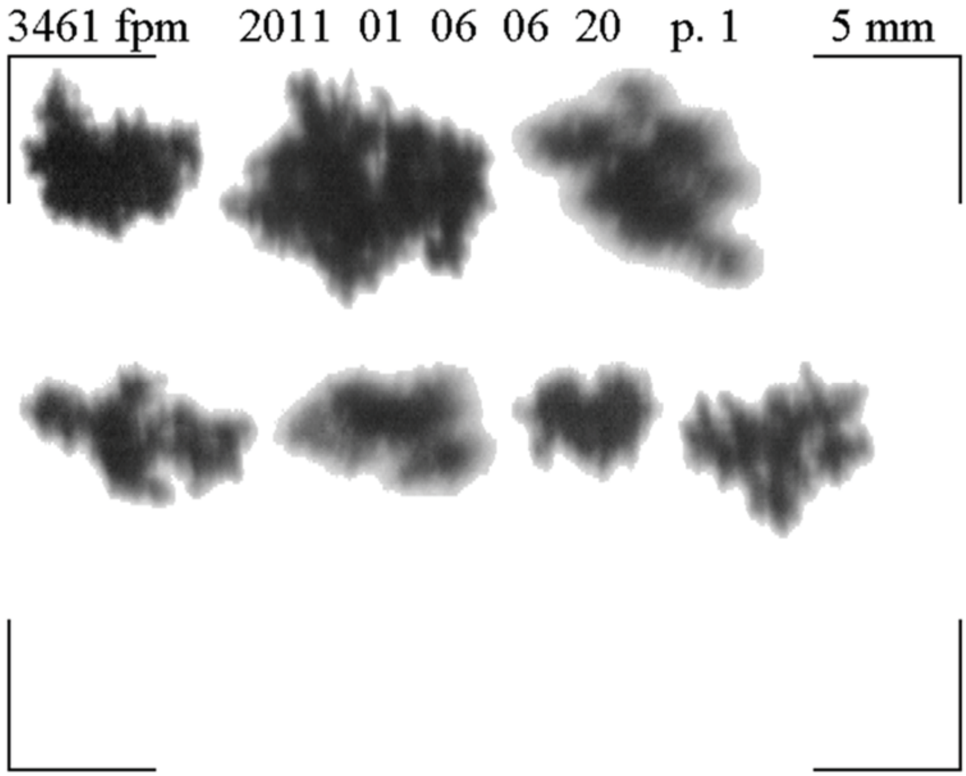

Fig. 18: Example of SVI images of large rimed aggregates at 0620 UTC on 06 Jan 2011 at Järvenpää site.

836

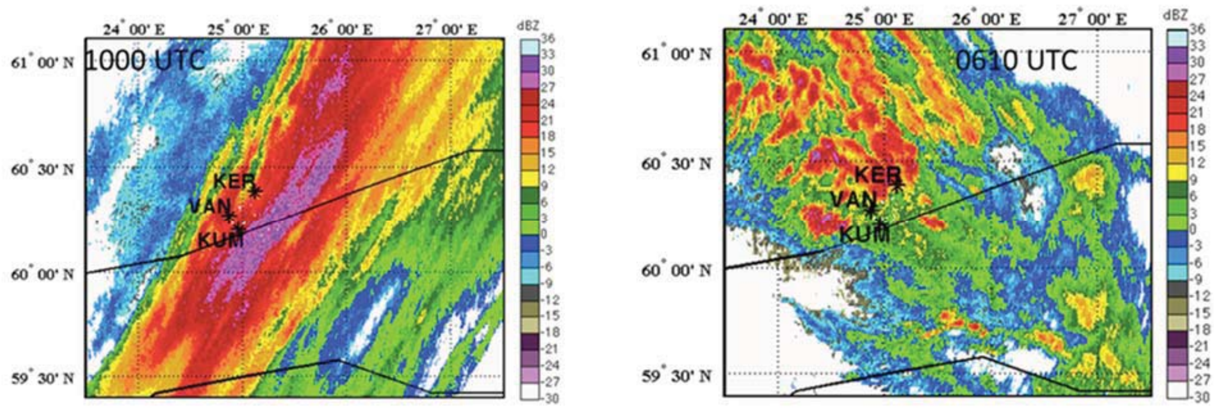

Fig. 19: Spatial variability of reflectivity (left panel) for 30 Dec 2010 and, (right panel) for 06 Jan cases.

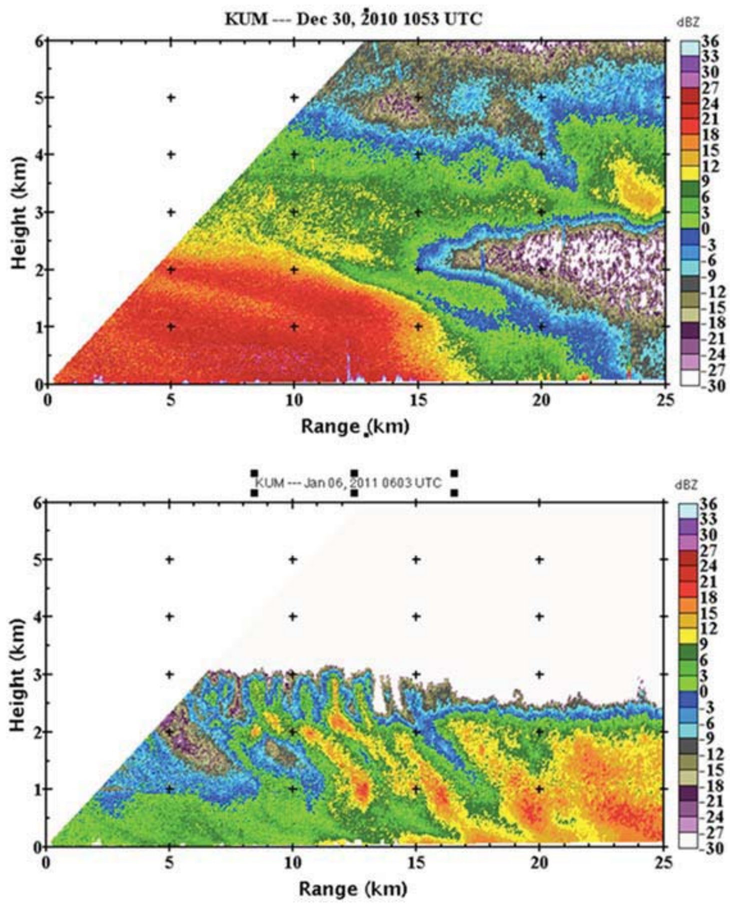

Fig. 20: RHI scan data from Kumpula radar along the radial to the Järvenpää site (top panel) 30 Dec 2010 at 1053 UTC, and (bottom panel) 06 Jan 2011 at 0603 UTC.

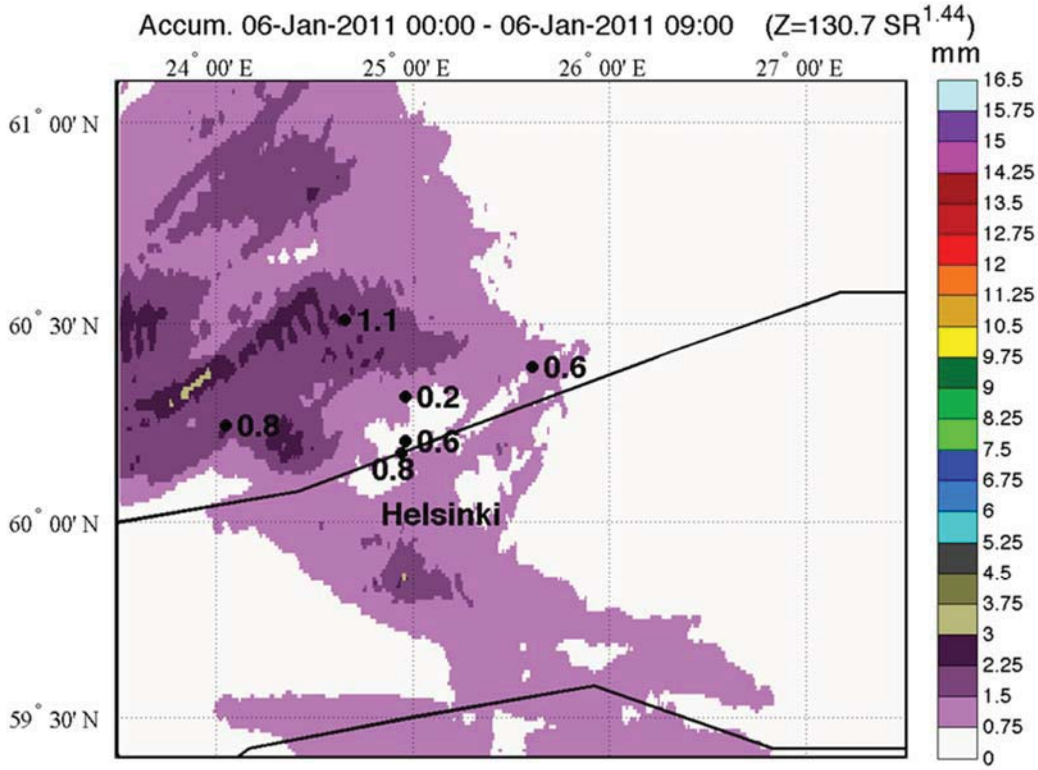

Fig. 21: As in Fig. 13 except for 06 Jan 2011 event (0000-0900 UTC only) using 2DVD-derived Z_e-SR relation.

LIST of Tables

Table 1: The four snow days from LPVEx

Event	Time (UTC)	Temperature C	2DVD accum (mm)	OTT-PLUVIO2 accum (mm)
30 Dec 2010	a.0800-1300 b.1500-2359	a. -9 b. -8	3.84	4.24
06 Jan 2011	0230-0830	-7	1.53	1.53
12 Jan 2011	a.0800-1230 b.2230-2359	a. -3 b. -3	3.36	2.05
13 Jan 2011	0000-0500	-4	2.77	2.73

Table 2: Coefficient α and exponent (β) of ρ-D_{app} power law fit (density in g cm^{-3} and D_{app} in mm)

Event	Time (UTC)	α	β
30 Dec 2010	a.0800-1300	a. 0.15	-0.86
	b.1500-2359	b. 0.15	-0.96
06 Jan 2011	0230-0830†	0.17	-0.79
12 Jan 2011	a.0800-1230	a. 0.23	-0.88
	b.2230-2359	b. 0.19	-0.8
13 Jan 2011	0000-0500	0.19	-0.8

† the 2DVD stopped working at 0824 on this day

Table 3: The $Z_e = a*SR^b$ power law for the four days. Note Z_e in $mm^6\ m^{-3}$ and SR in mm h^{-1}.

	a	**b**
30 Dec. 2010	210.72	1.63
06 Jan. 2011	130.72	1.44
12 Jan. 2011	209.20	1.67
13 Jan. 2011	134.86	1.81

† The power laws are derived for application to all events occurring during the day.

Table 4: The γ-adjustment factor and the V_f -D_{app} fit parameters [c d κ].

Event	Time (UTC)	γ	γ_{SVI}	c	d	κ
30 Dec 2010	a.0800-1300 b.1500-2359	a. 2.21 b. 1.94	a. 2.46 b. 2.57	1.20	1.54	1.16
06 Jan 2011	0230-0830	2.55	2.92	1.37	1.37	1.25
12 Jan 2011	a.0800-1230 b.2230-2359	a. 3.53 b. 2.23	a. 3.6 b. 2.18	1.37	1.85	1.78
13 Jan 2011	0000-0500	2.23	4.24	1.34	1.34	0.95

† The V_f- D_{app} fits are derived for application to all events occurring during the day (note: D_{app} in mm and V_f in m s^{-1}).